

Luminosity functions of globular clusters in five nearby spiral galaxies using HST/ACS images

Luis Lomelí-Núñez^{*}, Y.D. Mayya, L.H. Rodríguez-Merino, P.A. Ovando,
and D. Rosa-González

Instituto Nacional de Astrofísica Óptica y Electrónica, Luis Enrique Erro 1, Tonantzintla 72840, Puebla, Mexico

Accepted XXX. Received YYY; in original form ZZZ

ABSTRACT

We here present the luminosity function (LF) of globular clusters (GCs) in five nearby spiral galaxies using the samples of GC candidates selected in Hubble Space Telescope mosaic images in *F*435*W*, *F*555*W* and *F*814*W* filters. Our search, which surpasses the fractional area covered by all previous searches in these galaxies, has resulted in the detection of 158 GC candidates in M81, 1123 in M101, 226 in NGC 4258, 293 in M51 and 173 in NGC 628. The LFs constructed from this dataset, after correcting for relatively small contamination from reddened young clusters, are log-normal in nature, which was hitherto established only for the Milky Way (MW) and Andromeda among spiral galaxies. The magnitude at the turn-over (TO) corresponds to $M_{V0}(\text{TO}) = -7.41 \pm 0.14$ in four of the galaxies with Hubble types Sc or earlier, in excellent agreement with $M_V(\text{TO}) = -7.40 \pm 0.10$ for the MW. The TO magnitude is equivalent to a mass of $\sim 3 \times 10^5 M_\odot$ for an old, metal-poor population. $M_{V0}(\text{TO})$ is fainter by ~ 1.16 magnitude for the fifth galaxy, M101, which is of Hubble type Scd. The TO dependence on Hubble type implies that the GCs in early-type spirals are classical GCs, which have a universal TO, whereas the GC population in late-type galaxies is dominated by old disk clusters, which are in general less massive. The radial density distribution of GCs in our sample galaxies follows the Sérsic function with exponential power-law indices, and effective radii of 4.0–9.5 kpc. GCs in the sample galaxies have a mean specific frequency of 1.10 ± 0.24 , after correcting for magnitude and radial incompleteness factors.

Key words: galaxies: star clusters – galaxies: formation – galaxies: evolution

1 INTRODUCTION

Globular clusters (GCs) are among the oldest objects in the universe. Their relatively high luminosities ($M_V = -5$ to -10) and compact sizes (half-light radius of a few parsecs) allow them to be readily detectable in nearby external galaxies (Harris 1996). Their low metallicities ($\log[\text{Fe}/\text{H}] \lesssim -0.5$) and enhancements of α elements ($\log[\text{O}/\text{Fe}] \geq 0.20$) suggest that they are formed at very early epochs of galaxy formation (Binney & Merrifield 1998). The GC formation requires highly efficient star formation, usually associated with intense starburst activity (Bastian 2008). Star formation in the spheroids (early-type galaxies, spiral bulges and halos) represents one such activity in the early universe. Interactions and mergers between galaxies provided the next

epochs of star formation efficient enough to form massive star clusters such as GCs (Whitmore & Schweizer 1995). These intermediate-age clusters are similar in size and mass as the young massive clusters, also known as Super Star Clusters (SSCs), seen in presently active starburst regions (O’Connell et al. 1995). In the present work, we refer to as SSCs all those relatively younger clusters associated to disks of galaxies and reserve the word GCs to describe old clusters associated to spheroids. Because of their early formation, the properties of GC systems in galaxies provide important constraints on models of galaxy formation and evolution (Ashman & Zepf 1998).

A variety of GC system properties that are potentially relevant to cosmological theories of galaxy formation have been identified. These include, colour distribution (Larsen et al. 2001; West et al. 2004), luminosity function (Reed et al. 1994; Whitmore et al. 1995), radial density distribution

^{*} E-mail: luislomeli@inaoep.mx (LLN)

(Kartha et al. 2014; Bassino et al. 2006), specific frequency as a function of galaxy type (Harris & van den Bergh 1981; Peng et al. 2008), total number of GCs as a function of supermassive black hole masses (Burkert & Tremaine 2010; Harris & Harris 2011; Harris et al. 2014), and the nature of their size distribution (Kundu & Whitmore 1998; Larsen et al. 2001; Webb et al. 2012). These properties have been exhaustively reviewed in Brodie & Strader (2006).

Elliptical galaxies have been the most commonly used targets for the study of GC systems. This is principally because of the relative ease with which GCs can be identified when superposed on a smooth light distribution in these galaxies, as compared to the inhomogeneities inherent to the disks of galaxies. In addition, the identification procedure of GCs in disk galaxies has to take into account possible contamination from reddened young SSCs and intermediate-old (age ~ 1 –10 Gyr) SSCs. Correction of GC magnitudes and colours for the effects of dust in the interstellar medium also becomes more important in spiral galaxies, than in elliptical galaxies.

The most important characteristic of GC systems is the existence of bimodality in their colour distribution (Zepf & Ashman 1993; Gebhardt & Kissler-Patig 1999; Larsen et al. 2001). This bimodality is understood to be due to an underlying bimodal distribution of GC metallicities (Brodie & Strader 2006). Elliptical galaxies with well-determined metallicities confirm the existence of such a bimodal distribution in metallicities (e.g., Cohen et al. 1998; Usher et al. 2012). This has led to the division of GC systems into two sub-populations: red and blue, corresponding to metal-rich and metal-poor populations, respectively. These two sub-populations show differences in other properties, such as size and spatial distribution (Kundu & Whitmore 1998; Larsen & Brodie 2000a; Webb et al. 2012), suggesting possibly two independent formation channels of GC systems.

The GC luminosity function (GCLF) is another property that is well established in elliptical galaxies. GCLFs are described by log-normal distributions with $M_{0,V} = -7.40 \pm 0.25$ and $\sigma = 1.40 \pm 0.06$ (e.g., Reed et al. 1994; Whitmore et al. 1995). The GCLF is often suggested to be a universal function (e.g., Hanes 1977b; Richtler 2003) in elliptical galaxies, and have been used as a standard candle for the determination of distances to their host galaxies (e.g. Richtler 2003). Among spiral galaxies, the log-normal nature of LFs have been firmly established only in the Milky Way (e.g., Harris 1996; Bica et al. 2006) and Andromeda (e.g., Peacock et al. 2010), the only two spiral galaxies where GC system properties have been reasonably well-characterized, with values of $M_{0,V} = -7.33$, $\sigma = 1.23$ (Secker 1992; Reed et al. 1994) and $M_{0,V} = -7.6 \pm 0.15$, $\sigma = 0.82$ (Secker 1992; Reed et al. 1994), respectively. Within the errors of measurements, these values are in agreement with the TO found in elliptical galaxies (Ashman et al. 1994). Using the catalog of Harris (1996) with 143 GCs, Jordán et al. (2007) found $M_{0,V} = -7.40 \pm 0.10$, $\sigma = 1.15 \pm 0.10$ for MW. Fall & Zhang (2001) reproduced the log-normal form, as well as the TO value of the Galactic GCs by evolving dynamically clusters obeying power-law mass functions under the gravitational potential of the Milky Way. The uniformity in the TO values in spite of GC systems being constituted of two independently formed sub-populations puts strong constraints

on the formation scenarios of metal-rich and metal-poor sub-populations.

The total number of GCs in galaxies (N_{GC}) is another property that strongly constraints the formation scenarios of galaxies. Hanes (1977a) found that N_{GC} is proportional to the mass of its host galaxy and is independent of its morphology. Harris & van den Bergh (1981) defined the specific frequency, S_N , defined as the number of GCs per absolute magnitude in the V-band, normalized to $M_V = -15$ mag: $S_N = N_{GC} \times 10^{0.4(M_V + 15)}$. They found that S_N of a galaxy is approximately proportional to the total luminosity of the spheroidal component in the galaxy. Recent studies have shown that elliptical galaxies have a higher S_N as compared to that in spiral galaxies (e.g., Peng et al. 2008; Georgiev et al. 2010).

Classical models of formation of elliptical galaxies either by merging of disk galaxies or by the multi-phase dissipational collapse have serious short comings to explain all the above-discussed properties of GC systems. For example, the scenario of the formation of ellipticals by mergers of spiral galaxies predicts similar S_N values in ellipticals as compared to spirals. These models require the metal-poor population forming earlier than the metal-rich clusters. On the other hand, under the hierarchical scenario of galaxy formation, metal-rich GC systems formed in-situ in the parent galaxy, which are defined as the highest peaks in density fluctuations, whereas the metal-poor GC systems formed in low-mass halos and got accreted into host galaxy (Côté et al. 1998). The predictions from these latter models depend critically on the assumed GC system properties in spiral and dwarf galaxies, which are yet to be well established beyond the Milky Way and Andromeda.

For firmly establishing GC system properties in spiral galaxies, the GC sample should cover a substantial area of the galaxy, reaching limiting magnitudes fainter than the expected TO magnitudes. In addition, it is desirable to have observations in one of the filters bluerward of the Balmer jump (~ 3650 Å) at least in some fields in order to estimate the contamination of the GC sample by reddened SSCs. The first criterion requires analysis of multiple pointing Hubble Space Telescope (HST) images or ground based images taken with wide-field cameras, whereas the second one requires images deep enough to register $V \sim 23$ mag at distances less than 10 Mpc. The third criterion requires the availability of images in the U-band covering at least for some part of the target galaxies.

The existing works on spiral galaxies do not fulfil all the above three criteria. For example, Chandar et al. 2004 carried out a study of GCs in five spiral galaxies and Goudfrooij et al. (2003) of seven edge-on disk galaxies, both using HST/WFPC2 fields, but covered relatively small areas in each galaxy. Study by Young et al. (2012) of two edge-on spirals covered spatially their entire optical extents, but had a limiting magnitude slightly brighter than the expected TO. Other works on spiral galaxies include Santiago-Cortés et al. 2010 and Nantais et al. 2010b (M81; Sab), Hwang & Lee 2008 (M51; Sbc), Barmby et al. 2006; Simanton et al. 2015 (M101; Scd), Cantiello et al. 2017 (NGC 253; Sc) and González-Lópezlira et al. 2017 (NGC 4258 Sbc). None of these works fulfilled all the three criteria.

At present, multi-pointing HST data covering a good fraction of the galaxy angular size (see Figure 1) and ob-

Table 1. Sample of spiral galaxies

Name	Hubble Type	RA (J2000)	DEC (J2000)	A_V (mag)	R_{25} (")	a_{\max} (")	d (Mpc)	$m - M$ (mag)	Distance method	Source	M_{V_0}	$(B - V)_0$	Scale (pc)	Source SSCs	Proposal ID	Number of fields
(1)	(2)	(3)	(4)	(5)	(6)	(7)	(8)	(9)	(10)	(11)	(12)	(13)	(14)	(15)	(16)	(17)
M81	Sab	09:55:33.1	69:03:55	0.220	13.45	7.74	3.61	27.79 ± 0.06	Cepheids	1	-21.10	0.91	0.87	1,2	11570	29
M101	Scd	14:03:12.5	54:20:56	0.023	14.42	7.49	6.95	29.21 ± 0.06	Cepheids	2	-21.37	0.44	1.68	4,6,7	9490,9492	12
NGC4258	Sbc	12:18:57.5	47:18:14	0.045	9.31	8.60	7.576	29.397 ± 0.032	MASER	3	-21.03	0.67	1.84	3	1157	17
M51	Sbc	13:29:56.2	47:13:50	0.095	5.61	3.40	8.43	29.67 ± 0.02	SNII	4	-21.40	0.57	2.04	4,5	10452	6(4)
NGC628	Sc	01:36:41.7	15:47:01	0.192	5.23	5.1	9.77	29.95 ± 0.04	SNII	5	-20.75	0.50	2.36	4,8	10402	3

Notes: (1) Galaxy Name, (2) Hubble morphological type from RC3 (Corwin et al. 1994), (3,4) Right ascension, Declination, in J2000, (5): Galactic extinction from Schlafly & Finkbeiner (2011), (6) R_{25} from RC3 (Corwin et al. 1994), (7) a_{\max} is the angular size along the semi-major axis covered by observations, (8) Distance used in this work, (9) Distance modulus, (10) Distance estimation method, (11) Source of distances: 1.- Tully et al. (2013); 2.- Riess et al. (2016). 3.- Reid et al. (2019); 4.- Rodríguez et al. (2014); 5.- Olivares E. et al. (2010), (12,13) Absolute magnitude in V band and $(B - V)_0$ colour from RC3 (Corwin et al. 1994), (14) HST/ACS pixel scale in pc pixel⁻¹, (15) References to previous studies of stellar clusters: 1.- Santiago-Cortés et al. (2010); 2.- Nantais et al. (2010a); 3.- González-Lópezlira et al. (2017); 4.- Whitmore et al. (2014); 5.- Hwang & Lee (2008); 6 Barmby et al. (2006); 7 Simanton et al. (2015); 8 Adamo et al. (2017), (16) HST proposal number, (17) Number of ACS fields of each galaxy used in this work.

served in multiple filters exist for a number of nearby spiral galaxies. Some of these galaxies are also observed in the $F336W$ filter. A careful analysis of these images would be able to provide catalogues of GCs that are free from contaminating stellar and non-stellar objects, and with a good spatial coverage. In this paper, we analyse five giant spiral galaxies that fulfill all the criteria mentioned above, and are nearer than 10 Mpc.

In §2, we describe the sample of galaxies and the data used. In §3, we explain the detection and our criteria for selecting sample of GCs in the selected galaxies. Results of the completeness tests are presented in §4. Analysis and discussion of the properties of our GC samples is presented in §5. In §6, we give concluding remarks.

2 SAMPLE OF SPIRAL GALAXIES AND DATA

With the aim of comparing the properties of GC populations in spiral galaxies with those in elliptical galaxies, we searched for nearby giant spiral galaxies with multiple pointing HST Advanced Camera for Surveys (ACS) images in at least three optical broadband filters. Galactic GCs typically have half-light radius $r_h \lesssim 10$ pc (Harris 1996). At the spatial resolution of ~ 0.1 arcsec (image scale = 0.05 arcsec pixel⁻¹) offered by the ACS, majority of the GCs are more extended than the Point Spread Function (PSF) up to ~ 10 Mpc distances. Beyond this distance, GC selection would be heavily affected by incompleteness. Keeping this in mind, we looked for HST images of giant spiral galaxies at distances < 10 Mpc. We analysed such data for five galaxies. In Table 1, we list these galaxies along with their basic properties and source of images. All these galaxies have multiple pointing HST/ACS images in $F435W$ (B), $F555W$ (V), and $F814W$ (I) bands, covering a good fraction of their optical extent. In addition, all have at least one pointing in the $F336W$ (U) filter, which allows an estimation of the contamination of our GC catalogues by reddened SSCs.

The Hubble Legacy Archive¹ (HLA) provides images and photometric catalogues obtained with DAOPHOT² (Stetson 1987) and SExtractor³ (Bertin & Arnouts 1996).

These catalogues have been used by Whitmore et al. (2014) to study the luminosity function of star clusters in selected fields for a sample of 20 spiral and irregular galaxies. As a first step, we used these catalogues to select a sample of GCs. However, we noticed that the adjacent images had vastly different limiting magnitudes in some galaxies. A visual inspection of catalogued sources on the images suggested that the background values used in some images were inappropriate (see Appendix A). Since we are looking for a complete sample of GCs up to a given limiting magnitude, we decided to make our own catalogues on the downloaded images.

In Figure 1, we show the images of galaxies in $F435W$ band, with footprints superposed. In Tables 2 and 3, we give logs of observations for four of our galaxies in the optical and $F336W$ filters, respectively. Different columns tabulate pointing IDs, exposure times, zeropoints⁴ (c_0) in each filter. We also give the number of stars used for astrometry and RMS error in the coordinates. The fifth galaxy, M81, has been the subject of study previously by our group (Santiago-Cortés et al. 2010), and hence we directly use the GC catalog from that study.

3 SOURCE DETECTION AND CLUSTER SELECTION

We used images in $F814W$ band for detecting sources using SExtractor. The critical detection parameters used are: DETECT_MINAREA=5 pixel, DETECT_THRESH=1.4, BACK_SIZE=32 pixel and BACK_FILTERSIZE=3 pixel, where each pixel corresponds to 0.05 arcsec. Using these criteria, typically we obtained several tens of thousands sources in each frame. Elaborate filtering criteria need to be implemented to select GCs from this catalogue.

As discussed in the introduction, making a catalogue of GCs is more challenging in spiral galaxies as compared to elliptical galaxies. This is because, unlike elliptical galaxies, spiral galaxies show a lot of structures at the scale comparable to the size of GCs. These structures lead to a lot of spurious sources in the SExtractor catalogue. Filtering based on structural parameters (e.g. Mayya et al. 2008), colour (e.g. Fedotov et al. 2011), concentration index (e.g.

¹ <https://hla.stsci.edu/hlaview.html>

² <http://www.star.bris.ac.uk/~mbt/daophot/>

³ <https://www.astromatic.net/software/sextractor>

⁴ The zeropoints were obtained from ACS Zeropoints Calculator: <https://acszeropoints.stsci.edu/>.

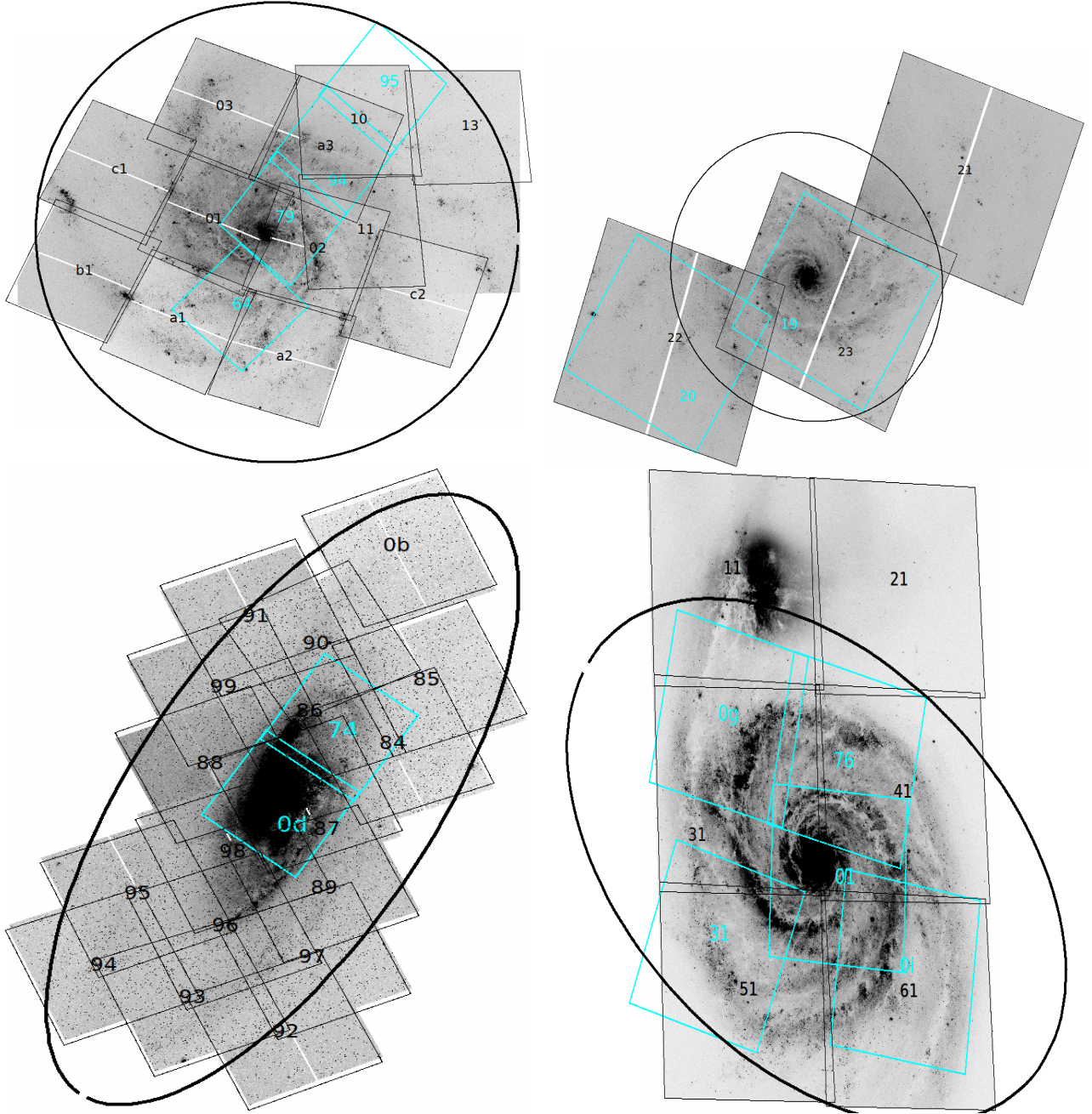


Figure 1. Sample of study. Galaxies are shown in $F435W$ filter, with observation footprints superimposed. Cyan-coloured rectangles show the $F336W$ filter footprints. The number in each footprint indicates the visit number within proposal. All galaxies are aligned such that north is up and east to the left. Black ellipse represent R_{25} for NGC4258 and M51, and $0.5R_{25}$ for M101 and NGC 628. See Figure 1 in [Santiago-Cortés et al. \(2010\)](#) for visualization of footprints in M81.

[Whitmore et al. 2014](#)), colour-colour diagrams (e.g. [Muñoz et al. 2014](#); [González-Lópezlira et al. 2017](#)) or a combination of these, are the most commonly used methods. In this paper, we used the cluster selection method used in [Mayya et al. \(2008\)](#) and [Santiago-Cortés et al. \(2010\)](#), which consists of using SExtractor-derived structural parameters (FWHM, AREA, ELLIPTICITY) to define a cluster sample, and photometric parameters (COLOUR) to separate young clusters from GCs. The method is described in detail in Sections 3.2 and 3.4, below.

3.1 Astrometric correction of HST images

Before running SExtractor it was necessary to astrometrize all HLA images. We performed this with the help of GAIA stars using Gaia Data Release 2 (Gaia DR2; [Gaia Collaboration et al. 2016](#); [Gaia Collaboration et al. 2018](#)). We used the IRAF task *ccmap* with a second order polynomial in coordinates to achieve this. Minimum of 10 stars were used in each pointing (5 stars in one pointing of NGC 4258), resulting in mean rms astrometric accuracies of ~ 0.095 arcsec (M101), ~ 0.014 arcsec (NGC 4258), ~ 0.048 arcsec (M51),

Table 2. Log of HST/ACS optical observations of our sample galaxies[†].

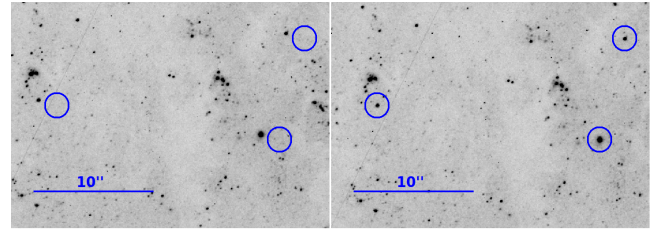
ID	<i>F435W</i>		<i>F555W</i>		<i>F814W</i>		Astrometric	
	T_{exp} (s)	c0	T_{exp} (s)	c0	T_{exp} (s)	c0	N_{stars}	RMS (arcsec)
M101								
01	900	25.792	720	25.736	720	25.531	93	0.0259
02	900	25.792	720	25.736	720	25.531	55	0.163
03	900	25.792	720	25.736	720	25.531	38	0.0385
a1	900	25.792	720	25.736	720	25.531	41	0.0319
a2	900	25.792	720	25.736	720	25.531	37	0.278
a3	900	25.792	720	25.736	720	25.531	11	0.0766
b1	900	25.792	720	25.736	720	25.531	10	0.187
c1	900	25.792	720	25.736	720	25.531	18	0.0925
c2	900	25.792	720	25.736	720	25.531	21	0.0175
10	1080	25.792	1080	25.736	1080	25.531	13	0.0988
11	1080	25.792	1080	25.736	1080	25.531	29	0.0456
13	1080	25.792	1080	25.736	1080	25.531	11	0.0862
NGC 4258								
0b	360	25.767	975	25.717	375	25.520	6	0.0134
84	360	25.767	975	25.717	375	25.520	8	0.0264
85	360	25.767	975	25.717	375	25.520	6	0.0058
86	360	25.767	975	25.717	375	25.520	27	0.0049
87	360	25.767	975	25.717	375	25.520	35	0.0049
88	360	25.767	975	25.717	375	25.520	26	0.0051
89	360	25.768	975	25.717	375	25.521	12	0.0023
90	360	25.767	975	25.717	375	25.520	13	0.0090
91	360	25.767	975	25.717	375	25.520	5	0.039
92	360	25.768	975	25.717	375	25.521	8	0.025
93	360	25.768	975	25.717	375	25.521	9	0.0273
94	360	25.768	975	25.717	375	25.521	9	0.03
95	360	25.768	975	25.717	375	25.521	8	0.0145
96	360	25.768	975	25.717	375	25.521	20	0.0157
97	360	25.768	975	25.717	375	25.521	8	0.0054
98	360	25.768	975	25.717	375	25.521	30	0.0054
99	360	25.767	975	25.717	375	25.520	14	0.0128
M51								
1-6	680×4	25.888	340×4	25.715	340×4	25.471	299	0.0482
NGC 628								
21	1200	25.789	1000	25.732	900	25.528	9	0.0445
22	800	25.788	360	25.731	720	25.528	15	0.047
23	1358	25.789	858	25.732	922	25.528	15	0.034

[†]Table 1 of [Santiago-Cortés et al. \(2010\)](#) contains observational log for 29 pointing in M81, the fifth galaxy of our sample.

and ~ 0.042 arcsec (NGC 628). We took into account these rms errors to identify and eliminate duplicate sources in the overlap zones between two adjacent frames. In Figure 2, we zoom in on an image section in M101 to illustrate a typical field before and after astrometric correction. The left image shows the HST coordinate system for this field, whereas the image on the right shows the corrected coordinate system. The circles show the coordinates of GAIA (Gaia DR2) stars in this field of view.

Table 3. Log of HST/WFC3 *F336W*-band observations of our sample galaxies.

ID	T_{exp} (s)	c0	N_{stars}	RMS (arcsec)	Proposal ID
(1)	(2)	(3)	(4)	(5)	(6)
M101					
64	2361	23.546	-	-	13364
79	2382	23.546	-	-	13364
94	2382	23.546	-	-	13364
95	2382	23.546	-	-	13364
NGC 4258					
0d	1062	23.546	33	0.0154	13364
74	1062	23.546	15	0.0109	13364
M51					
01	4360	23.546	163	0.0352	13340
0g	2376	23.546	55	0.0191	13364
0i	2361	23.546	42	0.0317	13364
76	2376	23.546	64	0.0281	13364
31	780	23.546	31	0.0350	14149
NGC 628					
19	2361	23.546	15	0.0031	13364
20	1119	23.546	10	0.0321	13364

**Figure 2.** Illustration of astrometry on the HST image using a section of M101. *Left:* astrometric coordinates on the downloaded image from HLA. *Right:* image after applying our astrometric corrections based on the GAIA DR2 coordinates of the field stars. Three field stars in the displayed FOV are identified with blue circles of 1 arcsec radius. North is up and east to the left in these images.

3.2 Selection criteria for defining a cluster sample

In this work, we aim to obtain a sample of GCs with properties similar to those in the Milky Way, which are marginally resolved on the HST/ACS images at the distances of sample galaxies. We considered all objects with $\text{FWHM} > 2.4$ pixel as GC candidates. This cut-off corresponds to 2.1 pc and 5.7 pc, in the nearest (M81) and farthest (NGC 628) galaxies of the sample. Thus, farther a galaxy is, lesser would be the number of compact objects we would detect. GCs do not show a mass-radius (or equivalently luminosity-radius) relationship ([Gieles et al. 2010](#)) and hence this bias is not expected to affect the LF of GCs. GCs are roundish objects, and hence their `ELLIPTICITY` parameter is expected to be close to zero. `SExtractor`-measured `ELLIPTICITY` even for roundish objects could be as high as 0.3, as it is measured at the isophote

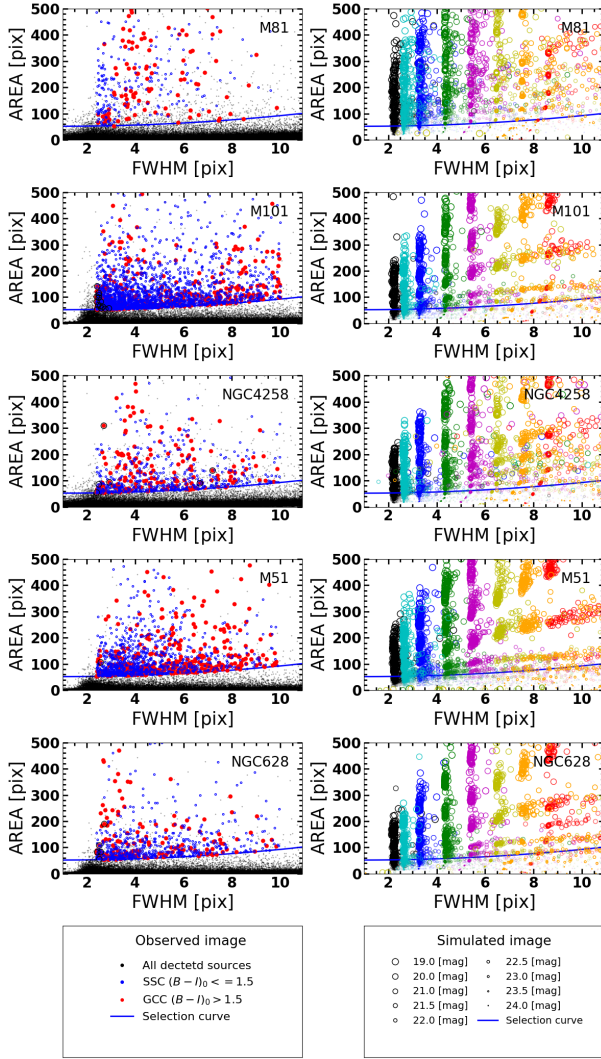


Figure 3. *Left:* Selected GCs (red dots) compared to all SExtractor sources (black dots) in AREA vs FWHM plane for our 5 sample galaxies. GCs have $(B - I)_0 > 1.5$ mag, $2.4 < \text{FWHM}/\text{pix} < 10$ and are above the parabola (blue line). Clusters bluer than this limit are SSCs which are identified by blue dots. Black dots above the parabola are extended sources with ellipticities > 0.3 , and hence do not satisfy all cluster selection criteria. *Right:* AREA vs FWHM for simulated star clusters. The FWHM of mock clusters are fixed at 2.0 (black), 2.4 (cyan), 3.0 (blue), 4.0 (green), 5.0 (magenta), 6.0 (yellow), 7.0 (orange) and 8.0 (red) pixels. For each fixed FWHM, 100 mock clusters between 19–24 magnitudes are generated, which are shown by symbols of different sizes (successively smaller sizes for fainter sources; see the bottom-most right panel for a guide on the symbol size). Most of the clusters with $\text{mag} > 23$ lie below the parabola defining the minimum AREA-FWHM relation, and hence are rejected by our selection criteria.

corresponding to the detection threshold on the background subtracted image. Another parameter that SExtractor calculates is AREA, which is the number of pixels enclosed by the isophote where ELLIPTICITY is measured. Both the ELLIPTICITY and AREA depend on the threshold used for the detection, and hence a cluster of same magnitude and FWHM can have different values of ELLIPTICITY and AREA, depending on the underlying background.

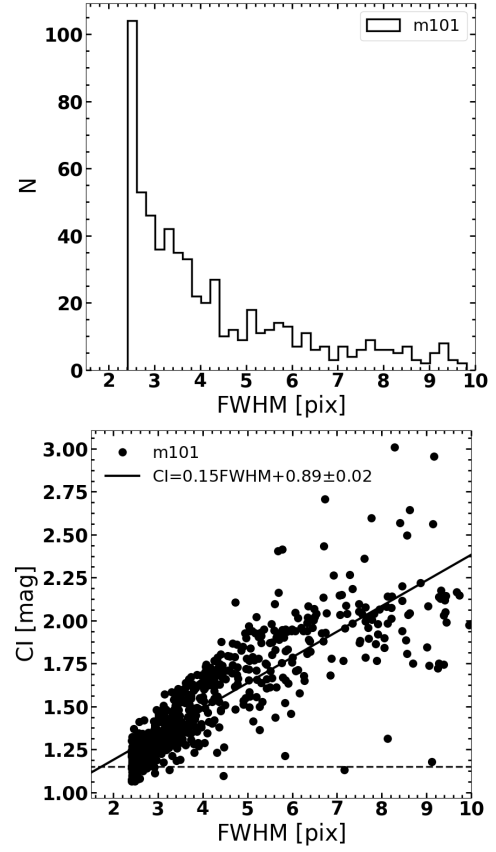


Figure 4. (Top) Distribution of FWHM for the candidate GCs in one of our galaxies (M101). (Bottom) Comparison of the two commonly used discriminators between clusters and stars, CI vs FWHM. Data are consistent with a linear fit (solid line whose equation is given in the top left corner) above the dividing line between clusters and stars (horizontal dashed line at $\text{CI}=1.15$). Data correspond to M101, which has 45 GCs below the defining line (see text for details).

We have carried out Monte Carlo simulations to understand the behaviour of these parameters for clusters of different FWHM and magnitudes, appropriate to the background and crowding encountered in each galaxy in the $F814W$ band. In Section 4, we describe in detail these simulations. In Figure 3 (right), we show the simulated clusters in AREA vs FWHM diagram for each of our sample galaxies. Simulations were carried out for a range of magnitudes between 19 and 24 magnitudes, for fixed values of FWHM. As expected, brighter clusters have larger AREAS at a given FWHM, and the AREA increases quadratically with FWHM for a cluster of given magnitude. We show the dependence of AREA with FWHM for objects of 23 mag by the blue solid curve, which is defined by the same equation, $\text{AREA} = 52.5 - 1.0 \text{ FWHM} + 0.50 \text{ FWHM}^2$, for all our sample galaxies. On the left panel, we show all the detected sources in FWHM vs AREA diagram for our five sample galaxies. The parabola defined by the simulations is shown, which separates the bonafide cluster candidates (that are above the parabola) from contaminating sources (image blemishes, stellar asterisms, image borders etc.), which dominate the number of detected sources at every FWHM. A hard

cut in magnitude or AREA can also eliminate the contaminating objects, but the use of parabola is the most effective way to eliminate these contaminating sources, without missing many genuine clusters. GCs at the distance of sample galaxies are expected to have FWHM close to the observational lower limit of 2.4 pixels. In the top panel of Figure 4, we show the observed distribution of FWHM for our final GC sample for one of our sample galaxies (M101), which indeed peaks at the first bin. However, we include objects up to FWHM=10 pixels to account for possible errors in the measurement of FWHM at detection limits. Simulations suggest that even the brightest clusters ($F814W = 19$) do not occupy an $AREA > 500$ pixels as long as the $FWHM \sim 5$ pixels, and hence we eliminated sources with $AREA > 500$ pixel.

The HLA catalogues include a parameter known as concentration index (CI), defined as the difference between magnitudes measured in 1 and 3 pixel radius apertures. Some studies have made use of this parameter to discriminate between point and extended sources (e.g., Whitmore et al. 2014, Simanton et al. 2015) $CI < 1.15$ for stars. In our study, we have used the $FWHM = 2.4$ pixel (0.12 arcsec), a direct discriminator between unresolved (stars) and resolved (extended) sources. In the bottom panel of Figure 4, we show CI against the FWHM for all our clusters for M101. As expected, the two parameters are correlated. The minimum CI (1.07) for our sample clusters is slightly less than 1.15, the value adopted in other studies. Forty-five ($\sim 4\%$) of our sources wouldn't have been classified as stellar cluster if we had adopted the CI criterion. A visual inspection of these borderline objects suggests they are likely to be clusters, rather than stars. We identify these borderline cases ($1.07 < CI < 1.15$) by red dots surrounded by black circles in Figure 8. In NGC 4258, these include two of the brightest GCs.

3.3 Aperture photometry

3.3.1 Magnitudes, colours and aperture correction

SExtractor was also used for obtaining photometry in the three bands for all the detected sources. The photometry was carried out in 10 apertures with radii between 1 and 15 pixel (0.05 arcsec to 0.75 arcsec), using the zeropoints (c0) tabulated in Table 2 for each frame. Unlike stars, aperture correction for clusters depend on the cluster size, which is parameterized by the FWHM in SExtractor. The aperture correction is defined as the difference between magnitude at 3 pixel (0.15 arcsec) radius and the magnitude at an infinite aperture ($\Delta F814W = m_{F814W}(3 \text{ pix}) - m_{F814W}(\text{tot})$). Even the most extended clusters (objects with Gaussian $FWHM=9$ pixel) contain more than 98% of their total flux within an aperture of 15 pixel radius, because of which we have used the magnitude in an aperture of 15 pixel radius as $m_{F814W}(\text{tot})$.

We used the results of our experiments with simulated clusters, described later in Section 4, to obtain the correction as a function of measured FWHM in each galaxy. The results are shown in Figure 5 for M101. A group of horizontally distributed points corresponds to the same input FWHM. The measured FWHM for fainter clusters tends to be systematically larger than the input FWHM, which is the reason for the horizontal spread. The aperture corrections (open cir-

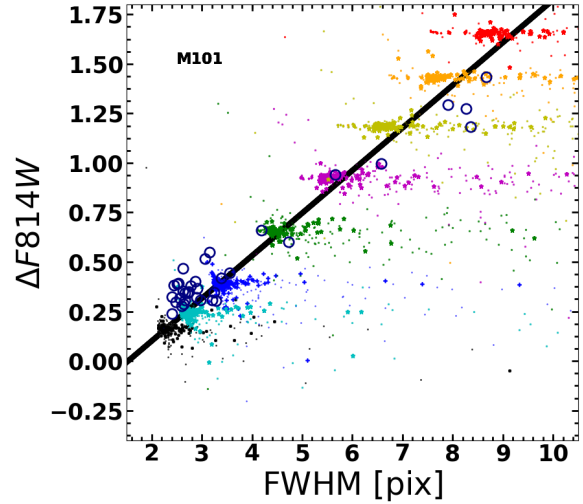


Figure 5. Apertures corrections vs FWHM for observed (open circles) and simulated (coloured points) star clusters in M101. The line is the linear fit to the simulated points.

Table 4. Aperture correction coefficients and typical photometric errors in $(F435W - F555W)_0$ colour for the sample galaxies.

Galaxia (1)	m (2)	b (3)	σ_{BV} (4)
M81	0.193 ± 0.004	-0.277 ± 0.026	0.10
M101	0.215 ± 0.004	-0.330 ± 0.025	0.21
NGC 4258	0.193 ± 0.007	-0.279 ± 0.045	0.10
M51	0.218 ± 0.004	-0.354 ± 0.024	0.16
NGC 628	0.225 ± 0.003	-0.358 ± 0.022	0.19

Notes: σ_{BV} is the average standard deviation estimated in the $(F435W - F555W)_0$ colour in bins of 0.2 mag in $(F435W - F814W)_0$ colour for clusters with $(F435W - F814W)_0 > 1.5$.

cles) obtained for 35 isolated clusters with good photometry (error < 0.005 mag in 9 pixel) is also shown in the Figure. Both the simulated and observed corrections smoothly increase with the FWHM. For the simulated data, we obtained mean values of measured FWHM and correction for each input FWHM and fitted these mean values by a straight line which is shown by the solid line. The fitted results (the slope m , and the abscissa, b) for all the sample galaxies are given in Table 4.

We applied these corrections to the $F814W$ aperture magnitudes of 3 pixel radius of all cluster candidates to obtain their total magnitudes. Colours ($F435W - F814W$, $F435W - F555W$ and $F555W - F814W$), however are obtained by subtracting magnitudes in the corresponding filters at 3 pixel radius aperture. This procedure ensures that errors on colours are smaller than the aperture corrected magnitudes. The errors on colours were calculated by quadratically summing the magnitude errors in the two bands forming a colour.

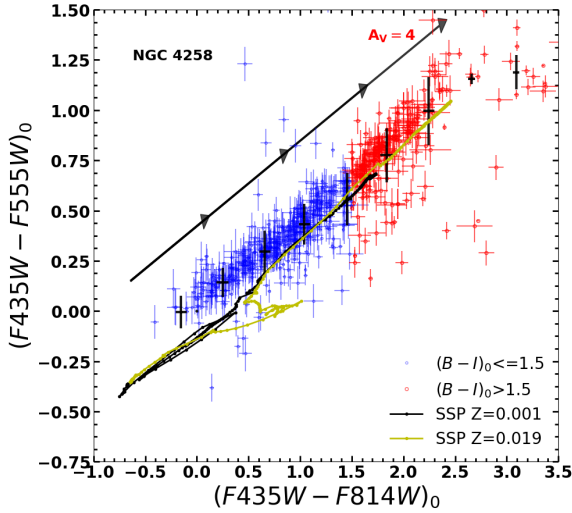


Figure 6. Colour-colour diagram showing all SExtractor-detected clusters for one of our sample galaxies (NGC 4258). The SSP evolution between 0 to 12 Gyr at two metallicities and the reddening vector for $A_V=4$ mag, with arrow heads placed at 1 mag intervals, are shown. Both the evolution and the reddening move the points along the same direction, and hence the spread in either axis around a mean local value (the crosses) is entirely due to observational errors in colours.

3.3.2 Photometric error estimation

Formal errors⁵ on photometric measurements are obtained using the formula: $MAGERR = 1.086 \times (FLUXERR/FLUX)$, where $FLUXERR = \sqrt{\sum_{i \in A} (\sigma_i^2 + \frac{p_i}{g_i})}$, with A representing the set of pixels defining the photometric aperture, σ_i , the standard deviation of noise (in ADU) estimated from the local background, p_i the background-subtracted image pixel value, and g_i the effective detector gain in e-/ADU at pixel i . However, small-scale variations in the disk background gives rise to additional errors while carrying out photometry of non-stellar objects such as GCs, that are usually larger than the formal errors. We use the colour-colour diagram $(F435W - F555W)_0$ vs $(F435W - F814W)_0$ to estimate the real errors on our colours. In Figure 6, we illustrate the method adopted for this. In this plot, we show the colours for star clusters in NGC 4258, with the SSPs with $Z=0.001$ and 0.019 metallicities from Bruzual & Charlot (2003). The reddening vector for $A_V=4$ mag is also shown. The reddening vector and the evolutionary trajectory are parallel in this colour-colour diagram, implying the spread in the $(F435W - F555W)_0$ colour for a fixed $(F435W - F814W)_0$ colour (and vice versa) is entirely due to observational errors. We calculated the dispersions in colour for each axis for fixed bins of 0.2 mag width in the other axis. In the figure, we show these dispersions by crosses placed at every 0.4 mag. There is a tendency for slightly higher error for the reddest colours. We take into account this dispersion in each colour as an additional source of error while comparing observational colours with model colours.

⁵ <https://sextractor.readthedocs.io/en/latest/Photom.html>

Table 5. Source detection and selection statistics.

Galaxy (1)	All N_{SSC+GC} (2)	N_{GC} (3)	N_{GC}^U/N_{GC} (4)	N_{cont}/N_{GC} (5)	N_{cont}/N_{GC} (6)
M81	565438	433	158	0.65	0.20
M101	1215533	3091	1123	0.14	0.32
NGC4258	1360607	626	226	0.35	0.35
M51	452747	1196	293	0.52	0.25
NGC628	224108	608	173	0.41	0.14

Notes: (1) Galaxy. (2) All sources (stellar+non-stellar+spurious) detected by SExtractor in all the pointings over the target galaxy. (3) Those sources satisfying the criteria explained in Section 3.2 to be identified as a cluster. (4) Subset of red $(B-I) > 1.5$ mag sources in column 3. (5) Fraction of total number CGs with photometry in an ultraviolet filter. (6) Fraction of contaminants (reddened SSCs) in our GC sample.

3.4 The sample of GCs

We define GCs as old (age > 10 Gyr) metal-poor ($Z \lesssim 0.001$) clusters, having properties similar to that for the sample of Galactic GCs. However, unlike the Galactic GCs, extragalactic GCs cannot be selected by their visual appearance even on the HST images. Our cluster sample contains GCs as well as relatively young clusters, such as SSCs. In Table 5, we list the source detection statistics in each galaxy. The second column contains all SExtractor-defined sources, with the column 3 containing the number of cluster sources. Cluster samples in spiral galaxies contain more SSCs than GCs, and hence quantitative criteria are required to discriminate between GCs and SSCs. Cluster colour is the most useful discriminator for achieving this. For example, metal-poor SSPs ($Z \leq 0.001$) predict $B-I \geq 1.5$ mag for populations older than ~ 3 Gyr (Bruzual & Charlot 2003).

In Figure 7, we plot the distribution of $(F435W - F814W)_0$ colours for all clusters (black histogram) and for clusters brighter than $M_{F814W} = -9$ mag (red histogram) in each galaxy. The latter is multiplied by a factor which is indicated in the figure annotation. For the bright cluster sample, four of the five galaxies studied here show a bimodality in the distribution, the exception being M101. The colour that separates the two distributions is nearly the same in all these galaxies, and corresponds to the $(F435W - F814W)_0 = 1.5$ mag bin. The full cluster sample also shows a minimum in the distribution close to this colour in four of the galaxies. In M101, although the evidence for bimodality is not strong for the bright cluster sample, the total sample indicates bimodality with the saddle point again corresponding to the $(F435W - F814W)_0 = 1.5$ mag. The blue and red distributions correspond to the SSCs, and GCs, respectively. Based on this, we use $(F435W - F814W)_0 = 1.5$ mag to separate GCs and SSCs. Column 4 of Table 5 lists the number of clusters classified as GCs using this colour criterion. Coordinates and photometry for each of the selected GCs are given in Table 6. The Table in the body of the text contains data only for three brightest objects in each galaxy. The entire Table is available in electronic version.

The red tail of the reddened SSC colours most likely extends beyond the colour cut of $(F435W - F814W)_0 = 1.5$ mag, and hence colour-selected GC sample in spiral galaxies is expected to have some contamination

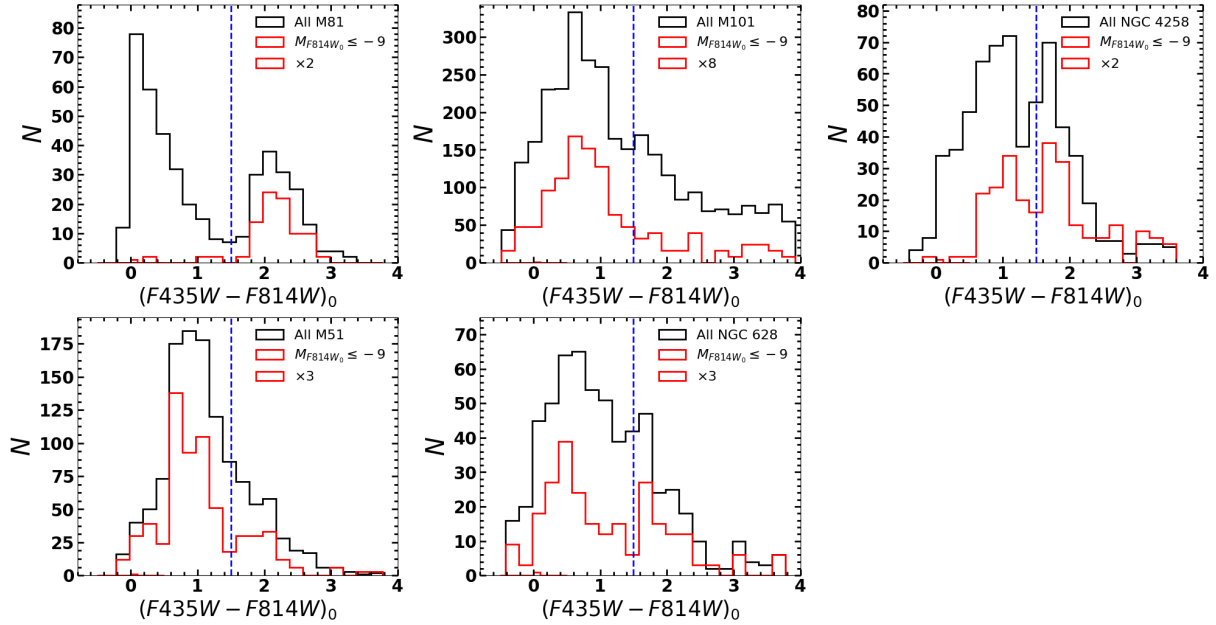


Figure 7. Colour histogram of all (SSC+GC) cluster candidates. The black line shows the colour distribution over the entire range of magnitudes, whereas the red histogram shows the distribution for bright ($M_I \leq -9$) clusters. The latter histogram values are multiplied by a factor indicated in each panel. The vertical line at $(F435W - F814W)_0 = 1.5$ separates SSCs from GCs.

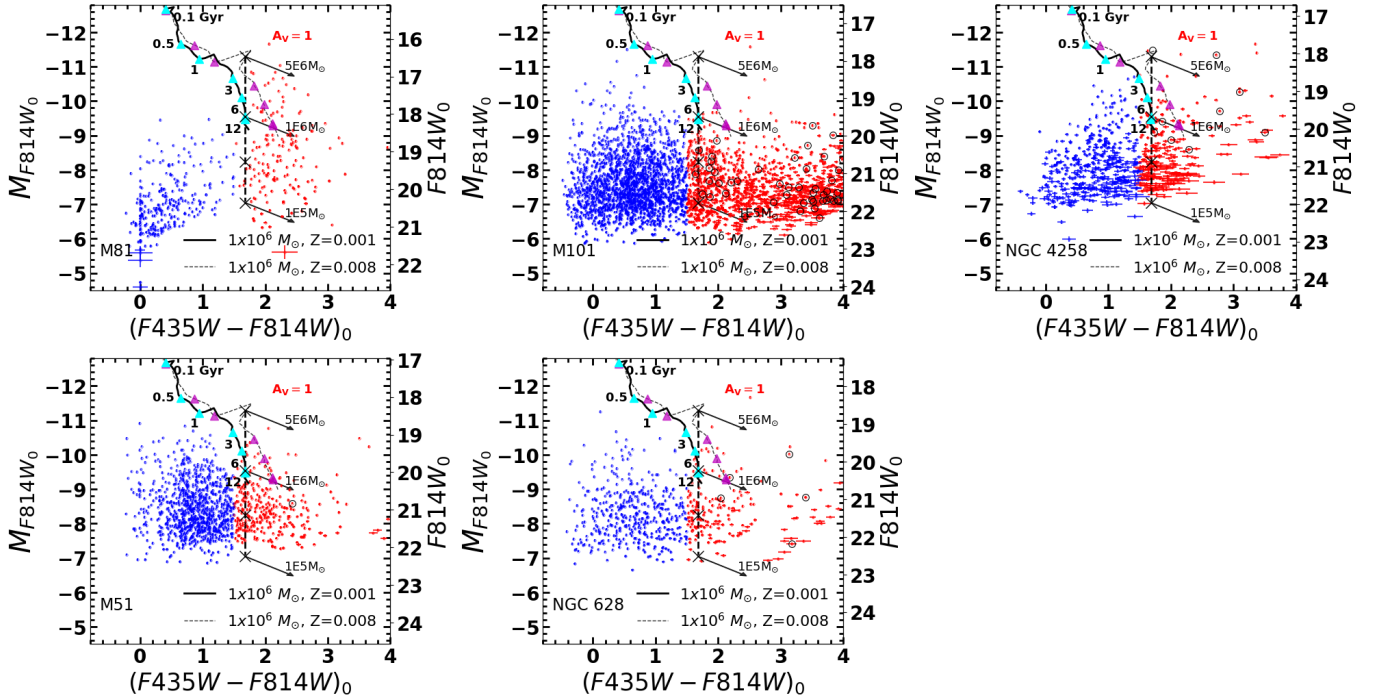


Figure 8. M_{F814W_0} vs $(F435W - F814W)_0$ CMD of all cluster candidates in our sample of galaxies. Candidates having $(F435W - F814W)_0 > 1.5$ mag are GC candidates (red dots), and bluer objects are young disk cluster candidates (blue dots). The evolutionary locus of the SSPs from [Bruzual & Charlot \(2003\)](#) for two metallicities ($Z=0.001$, black solid line and $Z=0.008$, black dashed line), of mass $=1 \times 10^6 M_\odot$ and Kroupa IMF, are shown. Locations corresponding to selected ages (0.1, 0.5, 1, 3, 6 and 12 Gyr) are marked (cyan and magenta triangles in each SSP). The chosen colour cut separates clusters older than 3 Gyr from the younger ones for unreddened SSPs. The reddening vectors with $A_V = 1$ mag are shown for 3 cluster masses for an SSP of 12 Gyr age and $Z=0.001$, typical values expected for GCs. The majority of the GC candidates are in the zone occupied by clusters of mass 1×10^5 to $5 \times 10^6 M_\odot$ and A_V between 0 and 1 mag. Encircled red dots correspond to compact GC candidates ($1.07 < CI < 1.15$; see section 3.2 for details) in our sample.

Table 6. Observational properties of the brightest three GCs in each sample galaxy.

ID (1)	RA (2)	DEC (3)	I (4)	$(B - I)_0$ (5)	$(B - V)_0$ (6)	$(U - B)_0$ (7)	FWHM (8)	AREA (9)	CI (10)	M_{F814W} (11)	r_{gc} (kpc) (12)	FLAG (13)
M81-GC1	148.84125	69.110425	16.13 \pm 0.03	2.06 \pm 0.10	1.10 \pm 0.10	1.63 \pm 0.10	3.62	-	-	-11.66	3.03	02
M81-GC2	148.94123	69.050097	16.75 \pm 0.03	2.24 \pm 0.10	1.27 \pm 0.10	2.05 \pm 0.10	3.45	-	-	-11.03	1.54	03
M81-GC3	149.11440	69.019380	16.95 \pm 0.03	1.78 \pm 0.10	1.00 \pm 0.10	1.43 \pm 0.10	5.82	-	-	-10.84	5.87	02
M101-GC1	210.824946	54.318723	17.63 \pm 0.02	2.51 \pm 0.00	1.20 \pm 0.17	1.31 \pm 0.41	3.07	449	1.30	-11.57	4.00	03
M101-GC2	210.884651	54.414166	18.57 \pm 0.02	2.74 \pm 0.00	1.14 \pm 0.17	-	3.38	394	1.50	-10.63	9.82	00
M101-GC3	210.884508	54.369237	19.10 \pm 0.02	2.48 \pm 0.00	1.46 \pm 0.17	-	2.92	301	1.39	-10.10	6.31	00
NGC4258-GC1	184.729270	47.264868	17.83 \pm 0.00	1.63 \pm 0.00	0.79 \pm 0.10	-	2.69	311	1.16	-11.57	5.25	00
NGC4258-GC2	184.865700	47.210389	17.89 \pm 0.00	3.37 \pm 0.01	1.13 \pm 0.10	-	2.79	165	1.18	-11.50	16.78	00
NGC4258-GC3	184.745970	47.301067	17.97 \pm 0.00	2.15 \pm 0.01	0.99 \pm 0.10	0.43 \pm 0.05	4.03	440	1.65	-11.42	0.69	02
M51-GC1	202.459584	47.174710	18.90 \pm 0.03	2.05 \pm 0.00	1.07 \pm 0.10	-0.06 \pm 0.17	3.10	462	1.44	-10.76	3.23	02
M51-GC2	202.507117	47.241845	19.18 \pm 0.03	3.50 \pm 0.00	1.52 \pm 0.10	1.17 \pm 0.17	2.77	271	1.35	-10.48	7.96	03
M51-GC3	202.469420	47.253906	19.31 \pm 0.03	1.75 \pm 0.00	1.25 \pm 0.10	-	2.47	281	1.24	-10.35	8.80	00
NGC628-GC1	24.221429	15.788914	18.28 \pm 0.03	2.51 \pm 0.00	1.08 \pm 0.16	1.82 \pm 0.07	3.33	471	1.56	-11.66	7.84	03
NGC628-GC2	24.171023	15.782500	19.13 \pm 0.03	1.90 \pm 0.00	0.68 \pm 0.16	0.28 \pm 0.09	2.75	243	1.37	-10.81	0.52	02
NGC628-GC3	24.212973	15.734987	19.71 \pm 0.03	3.15 \pm 0.00	1.25 \pm 0.16	-	2.62	183	1.16	-10.23	10.48	00

Notes: (1) Assigned name, which follows the convention of *GAL-GCn*, where *GAL* stands for galaxy name and *n* is 1 for the brightest object in the *F814W* filter, and increases sequentially as the magnitude increases. (2,3) Right ascension, Declination, coordinates in J2000. (4) Magnitude in *F814W*-band and magnitude error from SExtractor and aperture correction, added in quadrature. (5) $(F435W - F814W)_0$ colour, the error is the quadrature sum of the error in each band from SExtractor. (6) $(F435W - F555W)_0$ colour, error is quadrature sum as in column 5. In the case of M81 the colour is $(F435W - F606W)_0$. (7) $(F336W - F435W)_0$ colour, the error is the quadrature sum of the error in each band. In the case of M81 the colour is. $(u - g)_0$. (8) FWHM in pixel units from SExtractor. (9) AREA in pixels from SExtractor. (10) Concentration index, defined as the difference between magnitudes measured in 1 and 3 pixel radius apertures. (11) Absolute magnitude in *F814W*-band. (12) Galactocentric distance of the GC in kiloparsec. (13) FLAG classification: 00 clusters without *U*-band photometry; 01 determined as a reddened young cluster from *U*-band photometry; 02 - determined as bonafide GC from *U*-band photometry; and 03 - error in U-B is likely to be larger than the indicated formal error.

from the reddened SSCs. The SSC population has a long tail on the red side, which is either due to a spread in reddening, or/and due to a spread in ages of SSCs. In either case, the red tail of SSC distribution has very few clusters beyond $(F435W - F814W)_0 > 1.5$ mag. The estimation of contaminating objects in the GCs samples is discussed in Section 3.5.

In Figure 8, we plot all candidate clusters in a colour-magnitude diagram (CMD) formed using M_{F814W_0} vs $(F435W - F814W)_0$, where SSCs and GCs are shown by blue and red points, respectively. The evolutionary loci of clusters for Simple Stellar Population (SSP) models from Bruzual & Charlot (2003) at typical metallicities of SSCs ($Z=0.008\sim 1/3$ solar) and GCs ($Z=0.001$) are shown. These models correspond to synthetic clusters of mass = $1 \times 10^6 M_\odot$ obeying the Kroupa initial mass function (IMF) between masses 0.1 and $100 M_\odot$. If the GCs are as old as 12 Gyr, the range of magnitudes covered by the GCs corresponds to mass range shown by the dashed vertical line, and the range of colours corresponds to reddening equivalent to $A_V=0$ to ~ 2 mag.

3.5 Contamination of the GC sample from reddened SSCs

Figure 8 suggests that the reddened SSC colours overlap with the GC colours. The colour histogram (Figure 7) also suggests that the distribution of the SSC colours (the bluer peak) most likely has a long tail on the redder side, that overlaps with the GC colours. Thus, contamination to some degree from reddened SSCs is unavoidable when selecting GC samples in spiral galaxies using colour-cuts. We use the sub-sample of clusters with *U*-band photometry to estimate the fraction of contaminants in each galaxy.

Use of colour-colour diagrams involving ultraviolet and

optical filters is known to break the age-reddening degeneracy (e.g., Georgiev et al. 2006; Bastian et al. 2011; Fedotov et al. 2011). In particular, *U-B* colour separates clearly clusters younger (SSCs) and older (GCs) than ~ 3 Gyr. Keeping this in mind, we searched the HST archives for images in the WFC3/*F336W* filter. All our sample galaxies have at least one pointing in this filter (see Table 3). For M101, the *F336W* images had good astrometry. For the fields in other galaxies, we carried out the astrometry following the same procedure as described in section 3.1.

WFC3/*F336W* image for M81 is available for only one pointing, as compared to the 29 pointings with the ACS, with only 7 GC candidates (4%) falling in the FoV of the *F336W* image. The contamination fraction obtained from such a small coverage of the FoV is not expected to be representative. On the other hand, Sloan Digital Sky Survey⁶ (SDSS) image of this galaxy obtained from multiple pointings covers the FoV of all the 29 HST/ACS pointings. The relative nearness of this galaxy allows the detection and photometric analysis of 65% of clusters that occupy the relatively uncrowded fields. We hence used the SDSS *u - g* colours for estimating the contamination fraction in M81. In column 5 of Table 5, we present the fraction of GC candidates with *U*-band images, i.e. SDSS-*u* for M81 and HST/WFC3 *F336W* for the rest. We performed photometry using the *phot* task in IRAF using the same photometric parameters as for the HST/ACS images.

In Figure 9, we plot all candidate clusters with *F336W* coverage in $(F336W - F435W)_0$ vs $(F435W - F814W)_0$ colour-colour diagram. For M81, we show the SDSS *u - g* colours (in the AB system) in the ordinate. The evolutionary loci of clusters in this diagram for theoretical SSPs

⁶ <https://dr12.sdss.org/fields>

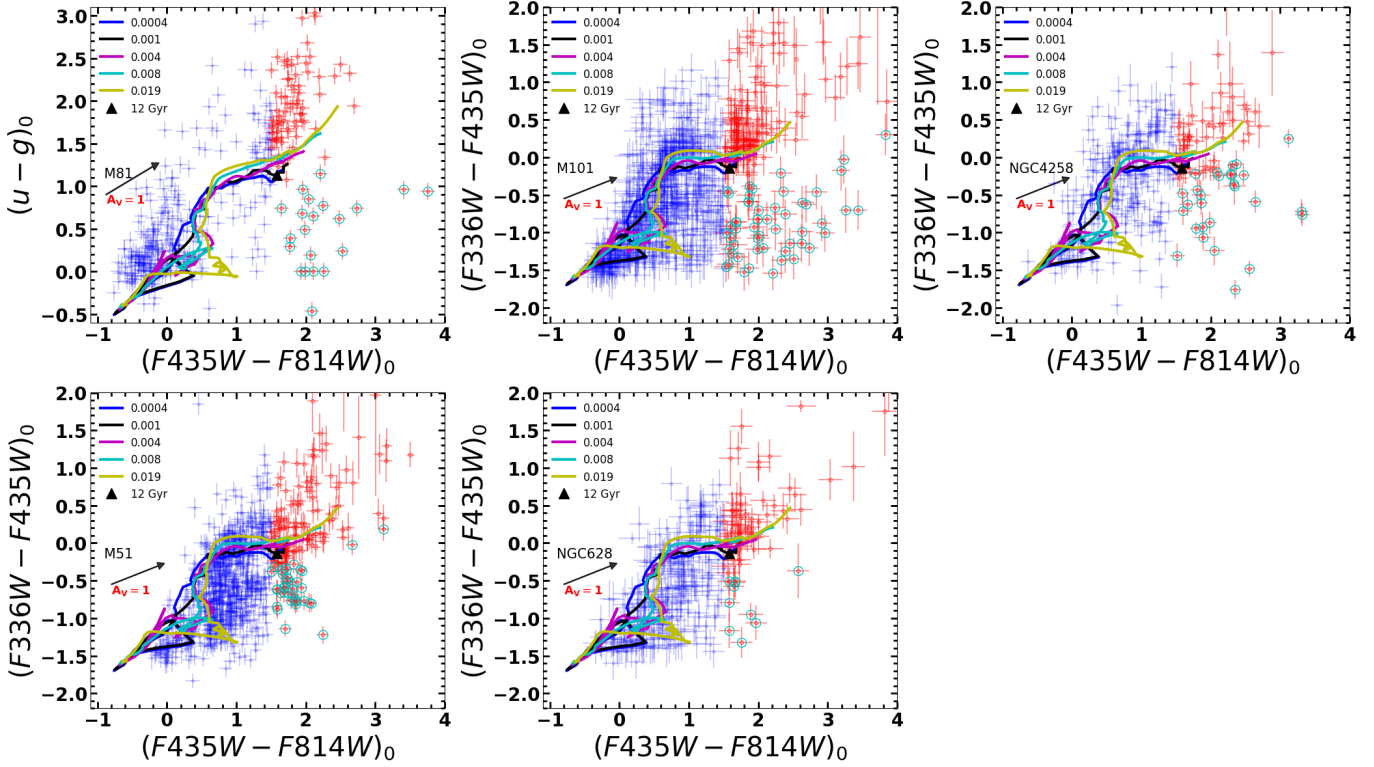


Figure 9. The U -selected cluster candidates in $(u-g)_0$ vs $(F435W - F814W)_0$ diagram for M81 and $(F336W - F435W)_0$ vs $(F435W - F814W)_0$ diagram for the rest of the sample galaxies. Candidates having $(F435W - F814W)_0 > 1.5$ mag are GC candidates (red dots), and bluer objects are young disk SSC candidates (blue dots). The evolutionary loci of SSPs from Bruzual & Charlot (2003) for different metallicities using Kroupa IMF are shown by solid curves of different colours, following the colour notation shown in each panel. The bluest colour that a classical GC can have ($Z=0.0004$ and age 12 Gyr) is marked by a solid triangle. The reddening vector with $A_V = 1$ mag is shown. The reddened young SSCs that occupy the GC colours are contaminants, which are identified by red dots surrounded by circles of cyan colour.

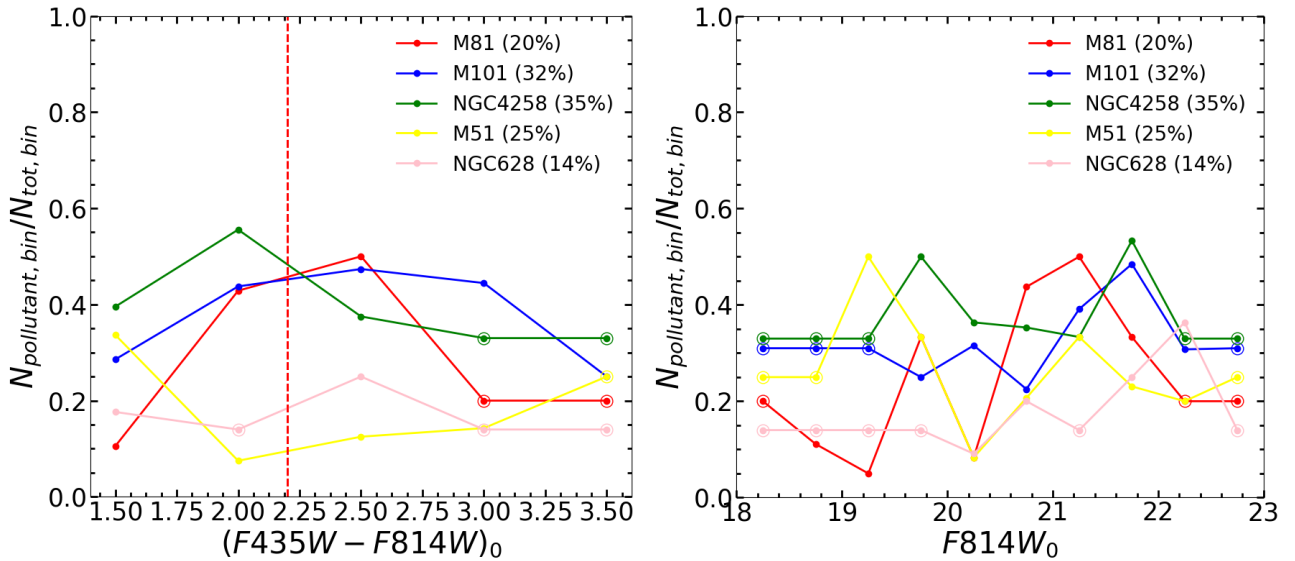


Figure 10. The fraction of contaminants (reddened young SSCs) in our GC samples as a function of colour (left) and magnitude (right) for our five sample galaxies. The vertical dashed-line in the left figure corresponds to the reddest colours reached by SSPs for unreddened GCs. See text for details.

from Bruzual & Charlot (2003) of different metallicities are shown. The $U - B$ colours of reddened young (< 10 Myr) clusters are distinctly different from that of clusters older than ~ 3 Gyr, which allows us to break the age-reddening degeneracy. Thus reddened young SSCs (contaminants) would lie below the SSP locus for age > 3 Gyr. In other words, for a redder ($F435W - F814W_0 > 1.5$) cluster to be considered a genuine GC, its $U - B$ colour, after taking into account photometric errors, should correspond to a location above the SSP locus in the figure. As illustrated in Figure 6, the real errors in photometry are larger than the formal error bars, which limits the use of the colours for a precise determination of age. Nevertheless, the photometric quality is good enough to separate reddened SSCs from GCs. In the last column of Table 5, we give the fraction of contaminants in our GC samples. The values lie between 14–35% in the sample galaxies.

In Figure 10, we explore whether contaminant fraction in our GC samples depends on the colour and magnitude of the GCs. We carry out this analysis in bins of 0.5 mag in colours and magnitudes. In order to avoid fluctuations caused due to small number statistics in some of the bins, we plot only those values for which the number of contaminants in any bin was more than the Poisson error in that bin, taken as the square root of the total number of GC candidates in that bin. For the rest of the bins, we plot the global values. In general, all galaxies have higher contaminant fraction for $(F435W - F814W)_0 > 2.2$ mag, with as much as 50% of the GCs of $(F435W - F814W)_0 = 2.5$ mag being contaminants (reddened young SSCs) in M101 and M81. None of the galaxies show any significant dependence of the contaminating fraction with magnitude. We hence use the global values of the contaminant fraction to correct the LF obtained from our entire GC sample in Section 5 for all galaxies.

3.6 Comparison of our GC catalogues with those in the literature

In four of our five sample galaxies, there exists a previous catalogue of GCs. We reiterate that none of these catalogues are as complete as our catalogues in terms of spatial and magnitude coverages, as well as in the estimation of contamination fraction from reddened SSCs. We here compare our catalogues, obtained using uniform selection criteria, with the catalogues from other authors, using different selection criteria.

M81: Nantais et al. (2010b) reported a sample of 233 GC candidates in M81, that had made use of data from HST/ACS and SDSS. They used a $\text{FWHM} > 3$ ACS pixel (0.15 arcsec) as the main discriminator. We find that 107 of our 154 GCs are present in the catalogue of Nantais et al. (2010b). Most of the remaining 49 GCs in our sample have $2.4 < \text{FWHM} < 3$ pixel, which is the main reason for their exclusion in Nantais et al. (2010b). Lower number of GCs in our sample as compared to that of Nantais et al. (2010b) is due to the more stringent filtering that we imposed in the selection of GCs.

M101: Similarly, using data from the HST/ACS, Simanton et al. (2015) reported a sample of 326 star clusters in M101. The selection was made using the concentration index and a colour cut. Their sample includes extended objects,

and hence they used a magnitude cut of $M_V \leq -6.5$ to define GCs, resulting in a sample of 98 GC candidates. We find that 48 are present in their sample of GC candidates. Reasons for us missing 50 of their objects are that 25 of these have $\text{ELLIPTICITY} > 0.3$, 19 do not meet the AREA criterion and the rest do not meet our FWHM criterion.

NGC 4258: González-Lópezlira et al. (2017) reported a sample of 39 GCs in NGC 4258 using near infrared (NIR) data from CFHT (Canada France Hawaii Telescope) over a large FoV ($1^\circ \times 1^\circ$), but based on seeing-limited ($\sim 0.7 \text{ arcsec}$) dataset. The selection of the GCs was carried out using the colour-colour diagram $u^*i'K_s$ ($(i' - K_s)$ vs $(u^* - i')$) (Muñoz et al. 2014). In comparison, our catalogue using HST/ACS images contains 226 GCs over a FoV of $\sim 12.3' \times 17.2'$. From a spectroscopic follow-up of the objects, González-Lópezlira et al. (2019) concluded that the selection based on colour-colour diagram has between 10 to 30% contaminants (e.g. Muñoz et al. 2014; González-Lópezlira et al. 2019). Our FoV includes 29 objects of González-Lópezlira et al. (2017), of which 23 are in our catalogue. Out of the 6 missing objects in our sample, two are confirmed to be GCs using spectroscopic data by González-Lópezlira et al. (2019), another two are dwarf galaxies, with the remaining one being a foreground star. Reason for the two of their GCs to be absent in our sample is that they do not satisfy our selection criteria.

M51: Star clusters in M51 were catalogued by Hwang & Lee (2008) using HST/ACS images. They used the SExtractor parameters stellarity, FWHM and ellipticity for star cluster selection. They created two subsamples, one with $2.4 < \text{FWHM} < 20$ and the other with $2.4 < \text{FWHM} < 40$ pixel, resulting in a catalogue of 8400 stellar cluster candidates. If we applied their colour discriminator ($(B - V) > 0.5$ and $(V - I) > 0.8$) in their catalogue we obtained a sub-catalogue of 224 red clusters, 214 of which have $\text{FWHM} < 10$ ACS ACS pixels. Only 85 of these objects are in our catalogue of 223 GCs. We searched our master SExtractor output catalogue to find out the reasons for we missing 139 of their objects, and found that 85 of these have $\text{ELLIPTICITY} > 0.3$, 15 do not meet the AREA criterion and the rest do not meet our FWHM criterion.

NGC 628: The last galaxy of our sample, NGC 628, has also been a target for cluster searches using HST images by Ryon et al. (2017). However, they reported only young and intermediate-age clusters, and no GCs.

4 COMPLETENESS CORRECTIONS

We aim to study GC luminosity functions in our sample galaxies. In order to do that, we need to take into account possible sources of incompleteness in our catalogues. Two principal sources of incompleteness in our study are: i) incompleteness in magnitude and ii) incompleteness in radial coverage even with multiple HST pointings. In this section, we describe the method we have followed to correct for these observational limitations and obtain a final GC luminosity function.

4.1 Monte Carlo cluster simulations

We generated mock clusters using the IRAF/DAOPHOT tasks *addstars* and *mkobjects*. A cluster is defined by an

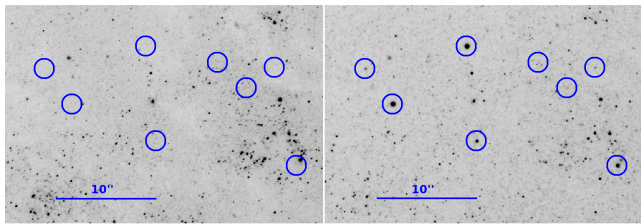


Figure 11. A randomly selected region of M101 before adding mock sources (left) and after adding them (right); sources have different magnitudes. All blue circular regions have 1 arcsec radius. North up, east left.

intensity profile that follows a Gaussian function of a given FWHM and a total magnitude, with FWHM taking values of 2.0, 2.4, 3.0, 4.0, 5.0, 6.0, 7.0 and 8.0 pixels, and magnitudes varying between 19 and 24 magnitudes at interval of 0.5 mag. For a fixed FWHM, 1100 clusters were generated, 100 for each simulated magnitude.

Coordinates of these sources were randomly selected and were inserted onto an observed HST image. The faintest object that can be detected in an observation under uniform background conditions defines the detection limit of that observation. In real observations, the background is often non-uniform, and each non-point source has a different size. Further, crowding of objects in an image can lead to non-detection of objects that are brighter than the detection limit. Hence, for each galaxy, we chose HST images corresponding to two FoV, representing zones of (i) low background and low crowding, and (ii) high background and high crowding. The former simulates the conditions typical of clusters in the external parts of galaxies, whereas the latter represents the characteristics of clusters in the bulge and spiral arms. For M81, which has as many as 29 pointings, simulations were carried out on an additional frame containing the bulge and nucleus (R09; see Figure 1 in [Santiago-Cortés et al. 2010](#), for the footprint of M81). The results of these latter simulations were used exclusively in the analysis of radial density distribution of clusters in the inner part of this galaxy. The same object detection and selection criteria (§3.2) we had used for real objects were applied on the mock-object added frames. In Figure 11, we zoom-in on a randomly selected region of M101, before (left) and after (right) inserting mock sources. In the image the positions of the mock sources, which cover a range of magnitudes, are indicated by blue circles.

We have also used these simulations to establish criteria to select cluster candidates from all sources catalogued by the SExtractor, and apply FWHM-dependent aperture corrections, described in Section 3.3. We used the results of the simulations for low background and low crowding for this purpose.

4.2 Completeness corrections: magnitude

For a proper counting of a population, it is necessary to know completeness factor as a function of object magnitude. We used the results of our simulation to determine the completeness factors. This factor is expected to depend on the FWHM.

Table 7. Magnitude at 50% completeness in *F814W*-band, for three curves in Figure 12

Galaxy	Low		High		Average	
	m_{50}	α	m_{50}	α	m_{50}	α
M81	22.93	3.74 ± 0.01	21.65	2.15 ± 0.04	22.32	1.08 ± 0.14
M101	22.72	3.79 ± 0.00	22.11	2.69 ± 0.16	22.44	2.05 ± 0.17
NGC 4258	22.60	4.02 ± 0.01	22.26	3.02 ± 0.00	22.46	2.96 ± 0.13
M51	22.92	3.24 ± 0.01	22.45	2.19 ± 0.00	22.69	2.07 ± 0.06
NGC 628	22.85	4.01 ± 0.01	22.72	3.97 ± 0.00	22.79	3.83 ± 0.01

Notes: m_{50} is the magnitude at 50% completeness and α is a fitting constant defined in Equation 1.

In the top panel of Figure 4, we plot the distribution of FWHM, which peaks at $\text{FWHM} < 3$ pixel. Hence, we calculate the completeness factors for mock clusters of input $\text{FWHM} = 3$ pixel. The completeness factor is defined as the ratio of the number of recovered objects (N_{out}) to the inserted objects (N_{in}) at each inserted magnitude.

In Figure 12, we show completeness curves in the *F814W*-band for all of our sample galaxies, for low (circles) and high (triangles) background frames. In order to quantitatively obtain the magnitude at which the sample is 50% complete, m_{50} , we fitted the points with the Pritchett function (e.g., [McLaughlin et al. 1994](#); [Alamo-Martínez et al. 2013](#); [González-Lópezlira et al. 2017](#)) given by:

$$f(m) = \frac{1}{2} \left[1 - \frac{\alpha(m - m_{50})}{\sqrt{1 + \alpha^2(m - m_{50})^2}} \right], \quad (1)$$

where α is a fitting constant that determines curve's slope. These fitted curves are shown by dotted and dashed lines, for low and high background frames, respectively. The GCs are distributed homogeneously across galaxies, including regions with a high and low crowding. To make the correction for incompleteness of the luminosity function, we decided to use the values of the mean curve, which is shown by the solid curve. In Table 7, the values for the 50% completeness for three curves are given for the *F814W*-band.

4.3 Completeness corrections: radial distribution

While the images obtained from HST observations offer the best spatial resolution, they do not cover the whole extent of galaxies even with the multiple pointings. Thus, outer halo GCs are often missing in catalogues selected from HST images. The following analysis was carried out to correct for the absence of GCs beyond the galaxy's disk.

GCs are the most easily noticeable objects in the halos of galaxies. However, their surface density in the inner parts always outnumbers that in the halos (see e.g. [Hargis & Rhode 2014](#); [Karthi et al. 2014](#)). In fact, the radial surface density distribution can be well described by the Sérsic function ([Sérsic 1968](#)) in its classical form:

$$N(R) = N_e \exp \left[-b_n \left(\frac{R}{R_e} \right)^{(1/n)} - 1 \right], \quad (2)$$

where, R_e is the effective radius enclosing half the population, n is the Sérsic index that controls the shape of the

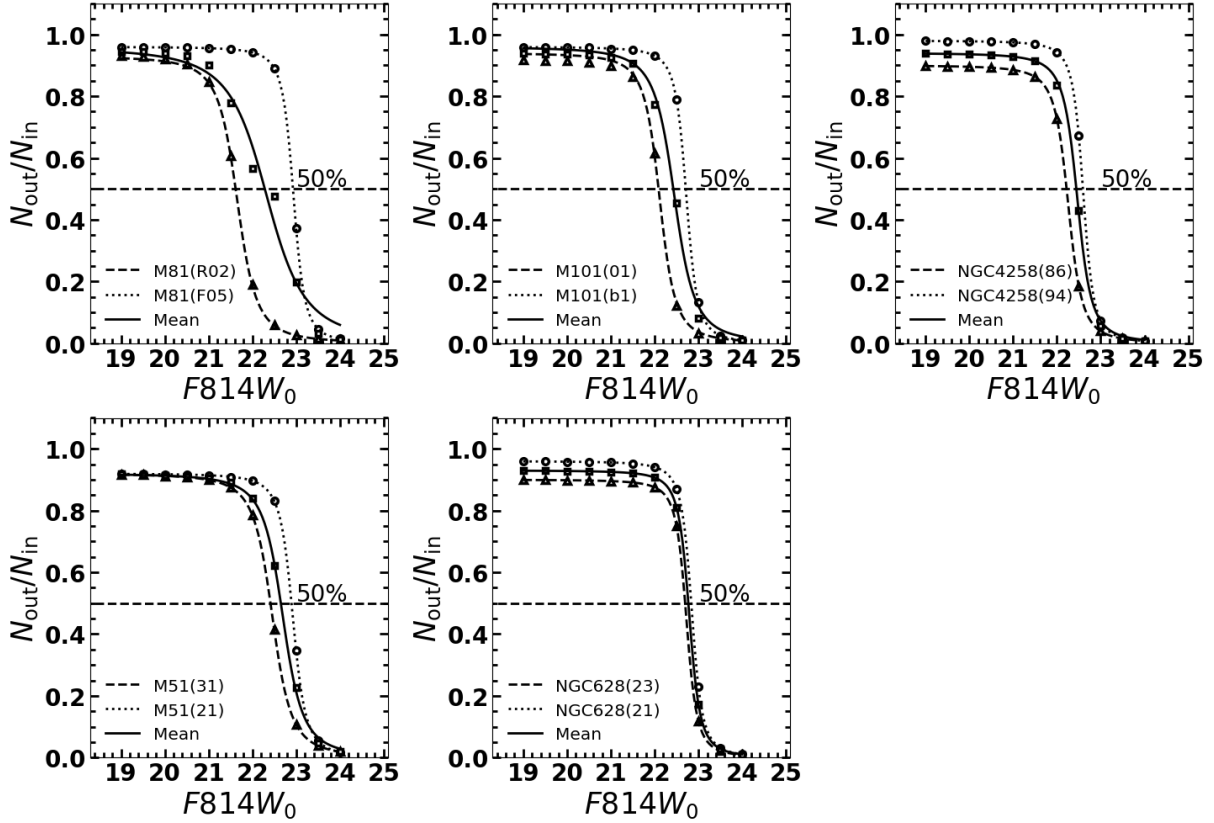


Figure 12. Completeness correction curves in the $F814W$ -band for our sample galaxies in low (dotted line passing through circles) and high (dashed line passing through triangles) background regions. The mean of these two curves is shown by the solid line. The identification codes of high and low background frames used in these simulations are shown in parenthesis.

profile and $b_n = 1.992n - 0.3271$. We show the radial distribution of surface number density in Figure 13. The radial axis is plotted in units of R_{25} . For two of our sample galaxies (M81: [Perlmutter & Racine 1995](#), and NGC4258: [González-Lópezlira et al. 2017](#)), GC searches have been carried out using the ground-based data that complement the HST data in the outer parts, which have also been shown (green empty circles). The observed and completeness-corrected values are shown in solid circles of black and magenta colours, respectively, with the fits to these data shown by solid lines of corresponding colours. The numbers inside and outside the R_e are corrected by the incompleteness factors corresponding to high and low surface brightness fields, respectively. For M81, the inner most number is corrected by the completeness factor obtained from simulation on the frame that included the bulge and the nucleus. The R_e values before and after the incompleteness corrections are shown by dashed vertical lines of black and magenta colours, respectively. The effect of correction is to marginally shift the R_e to lower values, which is noticeable only for NGC4258 and M51 in the figure. In Table 8, we show the values for Sérsic fit. N_{GC,R_e} and N'_{GC,R_e} are the numbers of GCs inside R_e before and after correction for contaminants. To estimate the total number of GCs (see Section 5.6), we use the number of GCs within R_e , (N'_{GC,R_e}).

The number density obtained wide-field ground-based surveys underestimates the number of GCs inside R_e by

more than an order of magnitude in both the galaxies with such data. In NGC4258, the slope of our fit in the external part agrees with the observed number densities from wide-field survey, with the absolute values marginally below our predictions. On the other hand, number densities obtained from wide-field survey in M81 remain constant over a large radial range, which are likely due to some selection biases in the survey. On the other hand, the wide-field survey suggests an excess of GCs in the external parts of this galaxy as compared to our predicted values. This excess could be due to contamination from foreground stars and unbound intergalactic GCs in the M81 group (see e.g. [Jang et al. 2012](#); [Ma et al. 2017](#)).

Two of the most well-studied spiral galaxies, the Milky Way and M31, have $n = 1.9$ and $R_e = 4.41$ kpc and $n = 1.6$ and $R_e = 4.59$ kpc ([Battistini et al. 1993](#)), respectively. In comparison, for elliptical galaxies the calculated values are larger, e.g., NGC 720 (E5): $n = 4.16 \pm 1.21$, $R_e = 13.7 \pm 2.2$ kpc; NGC 1023 (S0): $n = 3.15 \pm 2.85$, $R_e = 3.30 \pm 0.9$ kpc; NGC 2768 (E): $n = 3.09 \pm 0.68$, $R_e = 10.6 \pm 1.8$ kpc ([Kantha et al. 2014](#)). The n and R_e for our sample galaxies are in the range of expected values in spiral galaxies. The n values are < 1 in four of our galaxies, suggesting flatter distribution in the inner parts of our galaxies, as compared to the Milky Way and M31.

Table 8. Results of Sérsic profile fits to the radial distribution of GC surface density.

Galaxy	Observed				Completeness-corrected			
	n	R_e (kpc)	N_{GC,R_e}	N'_{GC,R_e}	n	R_e (kpc)	N_{GC,R_e}	N'_{GC,R_e}
M81	0.57 ± 0.07	4.29 ± 0.16	93 ± 11	74 ± 9	0.66 ± 0.12	4.04 ± 0.23	109 ± 5	87 ± 4
M101	0.33 ± 0.05	7.68 ± 0.28	635 ± 24	432 ± 16	0.36 ± 0.07	7.61 ± 0.32	802 ± 15	545 ± 10
NGC4258	1.81 ± 0.50	9.48 ± 2.02	179 ± 39	116 ± 25	1.63 ± 0.30	8.21 ± 0.96	197 ± 27	128 ± 17
M51	0.74 ± 0.15	10.07 ± 1.15	250 ± 31	188 ± 23	0.71 ± 0.12	9.54 ± 0.78	301 ± 20	226 ± 15
NGC628	0.48 ± 0.08	6.08 ± 0.27	113 ± 7	97 ± 6	0.48 ± 0.09	5.95 ± 0.29	149 ± 4	128 ± 3

Notes: R_e is the effective radius enclosing half the population, n is the Sérsic index from Equation 2. N_{GC,R_e} is the total number of GCs inside R_e , whereas N'_{GC,R_e} is N_{GC,R_e} after taking into account contamination from reddened young SSCs.

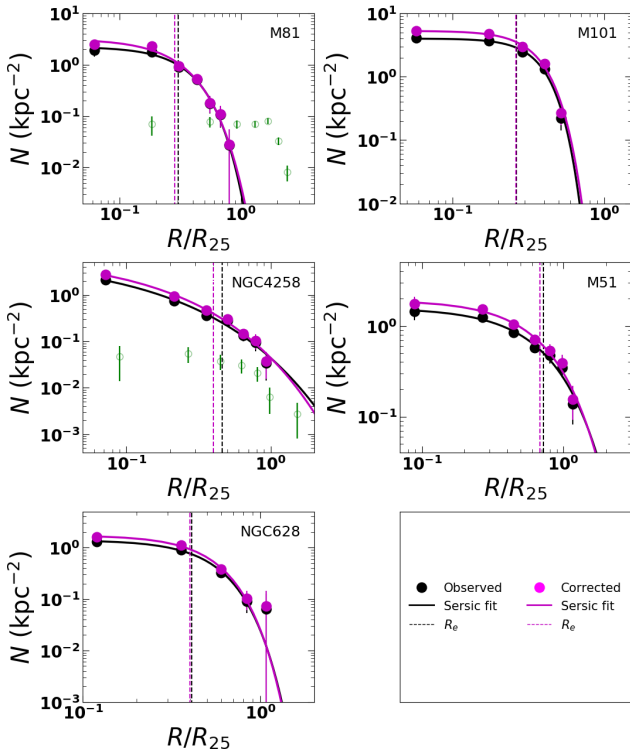


Figure 13. Radial distribution of surface number density of GCs from our data (solid circles) are fitted with Sérsic profile (solid line). Catalogued GCs beyond the spatial coverage of the HST images are shown by the empty circles (M81 and NGC4258, only). Observed number densities in these two galaxies are consistent with the extrapolation of the fitted function. The vertical dashed lines show the best-fit values of R_e before (black solid circles) and after (magenta solid circles) incompleteness correction.

5 GLOBULAR CLUSTER LUMINOSITY FUNCTIONS (GCLFS)

Having obtained a sample of GCs in 5 spiral galaxies, we now analyse the properties of the GC systems in these galaxies. All magnitudes and colours have been corrected for the foreground Galactic extinction using the A_V values given in Table 1, and the Cardelli et al. (1989) reddening curve. We start our analysis with the colour distribution.

Table 9. The mean and mode of the colour distribution of sample galaxies and the MW.

Galaxy	$(B-I)_0$		$(B-V)_0$		$(V-I)_0$		$A_V(\text{int})$	$A_V(\text{int})$
	Mean	Mode	Mean	Mode	Mean	Mode	Mean	Mode
(1)	(2)	(3)	(4)	(5)	(6)	(7)	(8)	(9)
M81	2.21	1.81	1.31	1.21	0.90	0.77	0.86	0.32
M101	2.49	1.68	0.96	0.65	1.54	0.98	1.23	0.15
NGC4258	2.02	1.64	0.92	0.81	1.11	0.87	0.60	0.10
M51	2.04	1.71	0.93	0.87	1.10	1.03	0.68	0.19
NGC628	2.11	1.58	0.72	0.63	1.39	1.00	0.73	0.01
MW	2.34	1.70	1.01	0.72	1.33	1.01	1.04	0.17
SSP	1.57		0.67		0.90			

Notes: (1) Galaxy name. (2–7) Mean and statistical mode of the indicated colours. (8–9) Internal visual extinction obtained from mean and mode $(B-I)_0$.

5.1 Colour distribution

For comparing colours of our GCs with those in the MW, we transformed all our photometry into the Johnson-Cousins photometric system using the transformation equation B1 and the corresponding coefficients in Table B1 in Appendix B, which were taken from Sirianni et al. (2005).

In Figure 14, we show the distributions of $(B-I)_0$, $(B-V)_0$ and $(V-I)_0$ colours of GC systems in our sample galaxies, where the sub-index 0 stands for Galactic reddening-corrected colours, using the A_V values in Table 1. For comparison, we also plot the colour histograms of the GCs in the Milky Way using the data from Harris (1996). The black and blue histograms correspond to the observed and dereddened colours, respectively. In Table 9, we list the mean and mode of the distributions of the three colours $(B-I)_0$, $(B-V)_0$ and $(V-I)_0$ for our sample as well as for the MW sample from Harris (1996). We use only 97 Galactic GCs which had integrated colours available in Harris (1996). For comparison, we list the colour of a SSP of 13 Gyr with $Z=0.001$, the typical metallicity of old GCs, in the last row. The reddening-corrected colours of MW GCs agree within 0.1 mag with these SSP colours.

The mode is systematically bluer than the mean in all the three colours in our sample galaxies as well as in the MW. This difference is due to a noticeable skewness in the colour distributions, with the peak (mode) occurring on the bluest bin in $(B-I)_0$ and $(V-I)_0$, in all cases except in M81. The skewness is not due to a colour cut we have

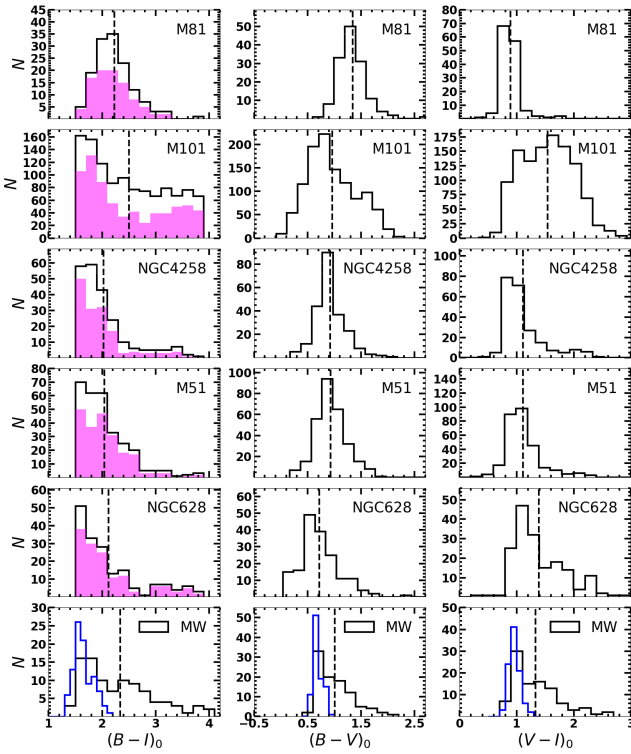


Figure 14. Colour distributions of GCs of our galaxies compared to that in the MW (bottom-most panels). The distributions of $(B - I)_0$ colour after correcting for contaminating fractions are shown by magenta histograms. The mean value for each distribution is shown by a vertical dashed line. The colour histograms after dereddening the colours by the reddening reported for each GC for the MW GCs are shown in blue.

used to define GCs. In fact the choice of the cut-off colour between SSCs and GCs corresponds to the saddle point in the distribution of colours of all cluster candidates (see Figure 7), with the peak in the GC colours occurring in the first or second bin redward of the saddle point. We analyse the possible role of contaminants in our GC samples to the origin of skewness in colour distributions. For this, we use the fraction of contaminants as a function of colour (see left panel in Figure 10) to correct statistically the $(B - I)_0$ colour histograms, which is shown in Figure 14 in magenta. The contamination-corrected histograms maintain the blue skewness in the distribution. This suggests that the skewness in colour distribution is an intrinsic property of the GC systems.

The mean and mode colours of our GC systems should correspond to SSP colours of metal-poor old clusters, if reddening is negligible. We find that the mode is only marginally redder than the colours of the metal-poor SSPs at old ages, whereas the mean is much redder. The redward shift of the mode from the expected SSP colours and the long red tail of the colour distribution, even for the MW sample, illustrate that the GC colours are often reddened by dust. The typical reddening experienced by GCs in each of our sample galaxies can be determined by comparing the mode of the colour distribution with the colour of the metal-poor old SSPs. We made use of the $(B - I)_0$ colour to obtain the colour excess $A_V(\text{int}) = ((B - I)_0 - (B - I)_{\text{SSP}})/(E_B - E_I)$,

where $(B - I)_{\text{SSP}}$ is the $(F435W - F814W)_0$ colour of the SSP, $E_B = 1.33$, and $E_I = 0.60$ are the values of the the Cardelli et al. (1989) extinction curve at the effective wavelengths of B and I -bands. The resulting values of $A_V(\text{int})$ using mean and mode are given respectively in columns 8 and 9 of Table 9. The $A_V(\text{int})$ obtained from the mode for our galaxies range from 0.01 (NGC 628) to 0.32 mag (M81) which is comparable to the 0.17 mag for the MW. The $A_V(\text{int})$ values obtained from the mean colours vary between 0.60 (NGC4 258) to 1.23 (M101), which is also comparable to the 1.04 mag for the MW.

The difference between the mean and median A_V values is ~ 0.5 – 1.0 in our sample galaxies, which is comparable to that for the Milky Way (0.87). Thus, GC systems in spiral galaxies experience relatively large mean extinctions. In fact, this is one of the reasons for the slow progress in establishing the properties of the GC systems in spiral galaxies. Some of the reddening could be due to dust internal to the clusters, whereas the majority is expected due to the dust along the line of sight in the disk of the host galaxy. The colour histogram in M101 shows a second peak at $(B - I)_0 \sim 3.5$ mag after correction for contaminants, suggesting the presence of a distinct red population. The analysis of LF below also suggests the presence of a population fainter than GCs. As we will see in Section 5.4, this population of faint red clusters corresponds to reddened intermediate-age (1–10 Gyr) SSCs. Under such a scenario, the basic assumption we have made in determining A_V , namely the clusters are old (> 10 Gyr) is not applicable to all clusters in M101 and hence the $A_V(\text{mean})$ would be an upper limit for this galaxy.

5.2 Luminosity function

We chose the Galactic extinction-corrected magnitudes in the $F814W$ band to construct the GCLF. For this purpose, we constructed histograms in bins of 0.5 mag over the entire range of detected magnitudes for each galaxy. The resulting histograms are shown in Figure 15 with red solid lines. The magnitudes corresponding to 50% completeness, m_{50} , at low and high surface brightness parts of for each galaxy are shown by dotted and dashed vertical lines, respectively. The observed numbers are corrected for incompleteness using the mean function shown in Figure 12. The corrected histograms are shown by gray bars. As expected, the correction factor is negligible at the bright end ($F814W \lesssim 21$ mag), and gradually increases at fainter magnitudes.

The GCLFs in the five galaxies show very similar form, increasing smoothly up to reaching a peak value, and then again decreasing smoothly. In other words, all our sample galaxies show a turnover, the TO. The TO values lie on the brighter side of m_{50} in all galaxies. The incompleteness-corrected histograms are fitted with a log-normal function given by:

$$dN/dM = N_0 e^{-(M - M_0)^2 / 2\sigma_M^2}, \quad (3)$$

where N_0 is a normalization factor, M is the absolute magnitude of the fitted bin, M_0 is the absolute magnitude of TO and σ_M is the dispersion. It can be seen that the log-normal functions are good fits to the observed LFs.

We obtained the TO magnitude after correcting the LF in each galaxy for a possible contribution from the contaminants. Following the discussions in Section 3.5, we used the

Table 10. Number of GCs and best-fit values for a log-normal distribution.

Galaxy	N_{GC}			TO			ΔTO	σ_M	$\Delta\sigma$	M_{814}^{1st}	M_{814}^{3rd}
(1)	Obs (2)	$\int LF$ (3)	total (4)	$F814W_0$ (5)	M_{F814W_0} (6)	M_{V_0} (7)	(8)	(9)	(10)	(11)	(12)
M81	126	128 \pm 13	177 \pm 15	19.56 \pm 0.12	-8.42 \pm 0.13	-7.52 \pm 0.16	-0.12	1.04 \pm 0.17	-0.11	-11.66	-10.84
M101	764	1325 \pm 60	1891 \pm 70	22.16 \pm 0.05	-7.14 \pm 0.08	-6.24 \pm 0.13	1.16	0.89 \pm 0.05	-0.26	-11.57	-10.10
NGC4258	147	166 \pm 31	290 \pm 51	21.19 \pm 0.11	-8.26 \pm 0.11	-7.36 \pm 0.15	0.04	0.97 \pm 0.15	-0.18	-11.57	-11.40
M51	220	261 \pm 24	536 \pm 44	21.44 \pm 0.07	-8.34 \pm 0.07	-7.44 \pm 0.12	-0.04	0.64 \pm 0.05	-0.51	-10.76	-10.35
NGC628	149	151 \pm 16	259 \pm 18	21.75 \pm 0.05	-8.21 \pm 0.06	-7.31 \pm 0.12	0.09	0.60 \pm 0.07	-0.55	-11.66	-10.23

Notes: (1) Galaxy name. (2) Number of GCs after correcting for contamination from reddened SSCs. (3) Column 2 after correcting for incompleteness in magnitude. (4) Estimated total number of GCs determined using Equation 6. (5) Observed TO magnitude in $F814W$ -band. (6) TO absolute magnitude in $F814W$ -band, corrected for galactic and internal extinction. (7) TO absolute magnitude in V -band ($M_{V_0} = M_{F814W_0} + (V - I)_{SSP}$; $(V - I)_{SSP} = 0.90$). (8) $\Delta TO = TO(\text{galaxy}) - TO(\text{MW})$ in the V -band, where $TO(\text{MW}) = -7.4$ mag. (9) σ_M , from the fit. (10) $\Delta\sigma = \sigma_M(\text{galaxy}) - \sigma(\text{MW})$, where $\sigma(\text{MW}) = 1.15$. (11) M_{814}^{1st} , magnitude of the brightest GC. (12) M_{814}^{3rd} , magnitude of third brightest GC.

magnitude-dependent contaminant fractions for NGC 4258 and constant contaminant fractions from the last column in Table 5 for the rest. The resulting plots for each galaxy are shown in the right panels of Figure 15 and the results are tabulated in Table 10. In order to determine the possible errors on the determined TO, we carried out 1000 Monte Carlo simulations, by adding a Gaussian noise to each bin of the histograms. For this purpose, we used the square root of the number in each bin as the σ of the Gaussian. The histogram resulting from each experiment is fitted by Equation 3, each time finding TO and σ_M . The rms values of these 1000 simulations are taken as the error on TO and σ_M .

In order to investigate the universality of the function, we converted the apparent TO magnitudes to the absolute values using the best-available distances for the sample galaxies (see Table 1), and corrected these magnitudes for internal extinction using $A_{F814W}(\text{int}) = 0.58 A_V(\text{int})$, where $A_V(\text{int})$ is taken from the last column of Table 9. The resulting values are also given in Table 10. All galaxies with the exception of M101 are consistent with $M_{I_0} = -8.21 \pm 0.06$ mag, with a mean $M_{V_0} = -7.41 \pm 0.14$ mag. The TO of M101 is 1.16 mag fainter. We will discuss this case separately in next section.

How does the mean value for the galaxies compare with the values for elliptical galaxies and the MW? TO value for the MW is $M_V = -7.40 \pm 0.10$ mag (from Jordán et al. 2007), which is almost identical to the mean value of $M_{V_0} = -7.41 \pm 0.14$ mag obtained for four of our galaxies. The individual differences of the TO magnitudes for our sample galaxies from that of the MW are given in column 8 of the Table 10. The differences are well within 1σ value in all these four galaxies. Hence, the GCLFs in four of our sample galaxies have the same TO as that in the MW. In comparison, M31 value of $M_{V_0} = -7.60 \pm 0.15$ obtained by Secker (1992) and Reed et al. (1994) is ~ 0.2 mag brighter than our mean value, which is marginally larger than the $1-\sigma$ error of our measurements. As pointed out earlier, TO for M101 is clearly different, which could be due to underestimation of distance, or an intrinsically different value of TO. This will be analysed in detail in the next sub-section.

Despite the near universality of the TO values, the σ_M of the log-normal function varies widely in the sample galaxies. These differences in widths are illustrated in Figure 16,

where we plot all the log-normal fits normalized to their peak values. The TO value along with its error for the Milky Way GCs is shown as a vertical band. In this figure we also show the positions of the brightest GC in each of these galaxies, as well as the position of the third brightest GC. It can be easily seen that the dispersion in the brightest and the third brightest clusters in these galaxies is much higher than the dispersion in the TO values, suggesting that the TO values are more universal than the magnitude of the brightest, or the third brightest GC, in galaxies. The brightest GC in our sample of five galaxies belongs to M81, which is discussed in detail in Mayya et al. (2013).

5.3 Distance errors and the universality of the TO

For obtaining the TO, we have used the distances tabulated in Table 1. The tabulated distances correspond to the most recent determination of distances using Cepheids for M81 and M101, and the MASER distance for NGC 4258. For M51 and NGC 628, SNII distances were used.

Using only the distances reported after the year 2000 in NED⁷, we found 56 independent measurements for M81⁸, 79 for M101⁹, 77 for NGC 4258¹⁰, 27 for M51¹¹ and 23 for NGC 628¹². The methods of distance measurements include those using Cepheids, MASER, tip of the red giant branch (TRGB), SNII-optical, and Tully-Fisher. We recalculated TO values for each of these measured distances, which are shown plotted against the corresponding distances in Figure 17. The value of TO for the best-determined distance (that in Table 1) is indicated by a thick circle, which is colour-coded according to the method that was used to

⁷ <https://ned.ipac.caltech.edu/>

⁸ https://ned.ipac.caltech.edu/byname?objname=m81&hconst=67.8&omegam=0.308&omegav=0.692&wmap=4&corr_z=1

⁹ https://ned.ipac.caltech.edu/byname?objname=m101&hconst=67.8&omegam=0.308&omegav=0.692&wmap=4&corr_z=1

¹⁰ https://ned.ipac.caltech.edu/byname?objname=ngc4258&hconst=67.8&omegam=0.308&omegav=0.692&wmap=4&corr_z=1

¹¹ https://ned.ipac.caltech.edu/byname?objname=m51&hconst=67.8&omegam=0.308&omegav=0.692&wmap=4&corr_z=1

¹² https://ned.ipac.caltech.edu/byname?objname=ngc628&hconst=67.8&omegam=0.308&omegav=0.692&wmap=4&corr_z=1

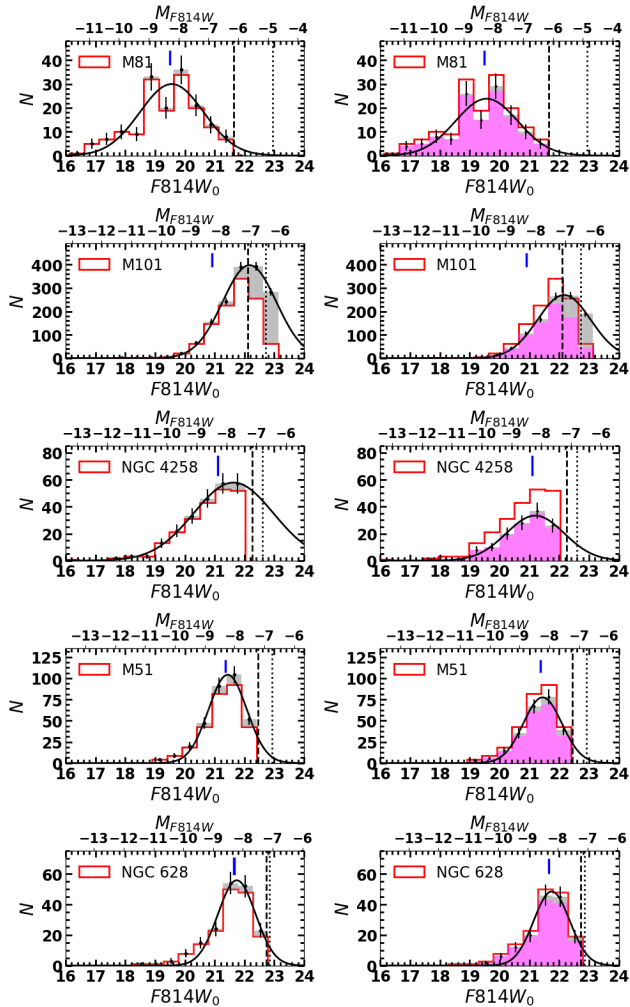


Figure 15. Best log-normal fits to the observed $F814W$ -band luminosity functions of GCs in our 5 sample galaxies. The data before (red histograms) and after (magenta-filled histograms) correction for possible contamination from reddened young SSCs are shown in the left and right panels, respectively. In each panel, fits were carried out to the completeness-corrected dataset (gray-filled histograms). Poisson error bars (\sqrt{N}) are indicated. The vertical dot and dashed lines indicate the magnitude at which the detection is 50% complete at low and high surface brightness parts of the galaxies, respectively. For reference, the turnover magnitude for the MW GCs is indicated in each plot by the blue vertical bar. The horizontal axes in the bottom and top contain observed and absolute magnitudes, respectively.

obtain the distance. The error on this best measurement is highlighted by the gray band. Most of the distance measurements for the 4 galaxies (M81, NGC4258, M51 and NGC628) agree with the value obtained by our best distance estimate, after taking into consideration the errors on each of them. In M101 where we found TO value fainter by 1.16 mag, some of the Cepheid distances are not consistent with the Cepheid distance (6.95 Mpc) we have used. If we use the farthest distance reported for this galaxy (8.99 Mpc, [Macri et al. 2001](#)), the TO value is still 8σ fainter than the universal value we have in other galaxies. Hence, we conclude that the TO value in M101 is intrinsically fainter compared

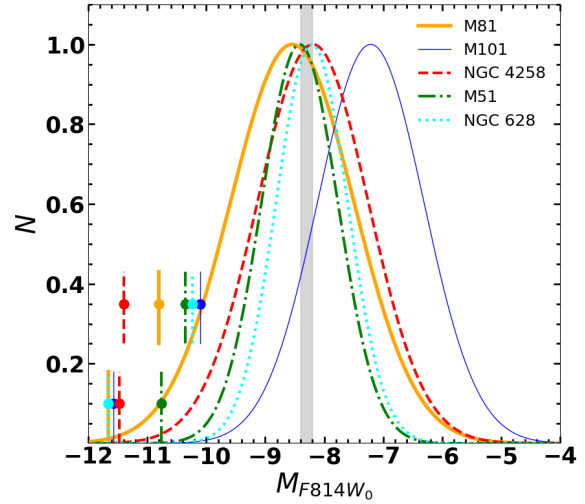


Figure 16. Comparison of the normalized $F814W$ -band GCLFs of all our sample galaxies. Line types and colours used for each galaxy are indicated. The TO magnitude of the MW GCs is marked by the gray band, with its width indicating the error on this value. The dispersion of the TO values in 4 of the galaxies (M101 is the exception) is smaller than the dispersion of their brightest GCs (bottom-most set of vertical lines) or the third brightest GCs (top set of vertical lines).

to that in other galaxies of our sample, and investigate the possible physical reasons for this difference.

5.4 TO magnitude in M101 and late-type galaxies

Among the galaxies analysed in this study, M101 stood out from the rest for having a fainter derived TO value, as well as for having a large population of very red clusters ($(F435W - F814W)_0 > 2.2$ mag), including a second peak at $(F435W - F814W)_0 > 3.5$ mag in its colour distribution (Figure 14). We here discuss whether these differences are related to its late morphological type (Scd). In Figure 18, we plot the TO values with respect to that in the MW as a function of the morphological type of the host galaxies. In this plot, we include the MW, M31 and the Large Magellanic Cloud (LMC). We estimated the TO in the LMC using data from [Mackey & Gilmore \(2003\)](#) for clusters with age ≥ 1 Gyr. TO values in all galaxies with morphological type Sc or earlier are in agreement with the value in the MW within the errors of measurements. The two galaxies later than Sc deviate from this trend. Thus, there is an indication that the different TO value found in M101 is indeed related to its late morphological type. In the following paragraphs, we discuss a possible scenario that naturally explains the fainter TO in late-type galaxies.

Classical GCs are among the oldest objects in galaxies, and their formation is related to the formation of halo and bulge ([Brodie & Strader 2006](#)). By definition, the prominence of these spherical components in galaxies decreases along the Hubble sequence. For this very reason, most of the searches of GCs were traditionally carried out in elliptical and early-type galaxies. Such studies have found relatively larger population of classical GCs in ellipticals as compared to that in spiral galaxies (e.g., [Harris & Harris 2011](#); [Harris et al. 2013](#)). On the other hand, M101 has a weak bulge,

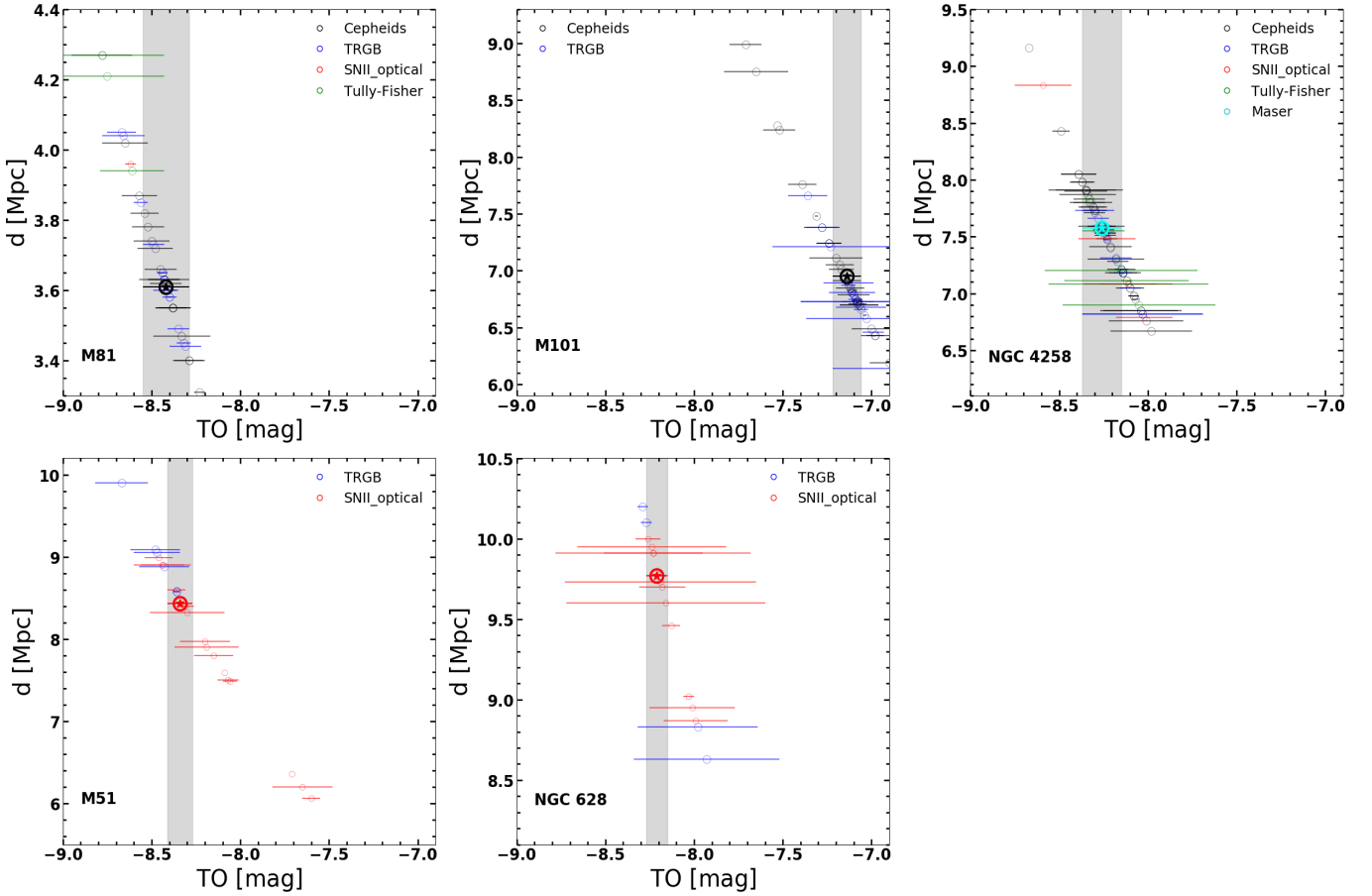


Figure 17. Dependence of the measured TO (circle) on the distance uncertainties. The measurement error on TO is shown by the width of the vertical gray band. Symbols in each plot are colour-coded depending on the method of distance determination.

classified as a pseudobulge by [Kormendy et al. \(2010\)](#), and a very poor stellar halo population ([Jang et al. 2020](#)), as expected for its late morphological type. These late-type systems are not expected to contain a large population of classical GCs. However, searches of GCs on HST images, including this study, find as many GCs in late-type galaxies as in early-type spirals. It is likely that not all the inferred GCs in late-type galaxies are classical GCs. We analyse this issue below.

Spiral and irregular galaxies are known to contain old SSCs that were formed in their disks and have survived the tidal shocks of their host galaxies. For example, [González-Lópezlira et al. \(2019\)](#) found that some of the objects classified as GCs in NGC 4258, one of the galaxies analysed in our study, belong to its disk and share the same kinematics as the disk HI gas. Formation and growth of galaxies through hierarchical merging, expects formation of such clusters during every epoch of merger involving gas-rich galaxies ([Mamikonyan et al. 2017](#)). The selection filters used for GC searches on HST and ground-based images do not distinguish these old stellar clusters from the classical GCs. Thus generally speaking the sample of objects observationally classified as GCs contains two kinds of objects, classical GCs related to the spherical component of galaxies, and old disk star clusters, formed *in-situ* or accreted onto, during

galaxy mergers as part of the hierarchical growth of galaxies. It is the former one that is expected to have universal TO. The fraction of old star clusters is expected to increase towards later Hubble types as they are more gas-rich than the early types. Hence, the TO obtained in early-type spirals represents that of the classical GCs, whereas in late-type galaxies it represents the population of old SSCs in the disk. This is found to be true in the LMC, where 50% of the old cluster population that is used to obtain the TO has ages in the 1–10 Gyr range.

In Section 3.5, we have estimated the contamination fraction from reddened SSCs in our sample of GCs in each galaxy, using the photometry in the *U*-band. The technique we have used helps to distinguish reddened SSCs from GCs only for SSCs younger than ~ 3 Gyr. Thus, our GC samples, in principle, contain all clusters older than ~ 3 Gyr. The universality of the TO in all our galaxies earlier than Sc, suggests that these early-type spirals did not form significant amount of SSCs after the formation of halo and bulge, or even if they are formed, they did not survive the gravitational shocks.

The GC population in M101 has been the subject of study by [Simanton et al. \(2015\)](#). They found a total of 326 candidate GCs, with their luminosity function matching very well the LF for the Galactic GCs, but starts increasing

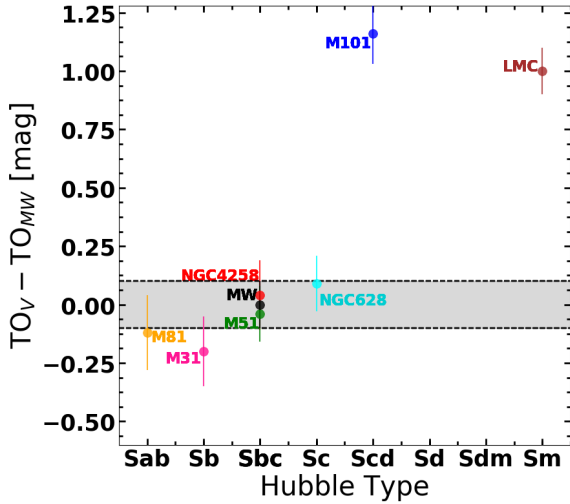


Figure 18. $TO_V - TO_{MW}$ vs the Hubble Type of host galaxies. The plot includes our 5 sample galaxies, and other spiral (M31) and irregular (LMC) galaxies where such measurements are available. The error in the MW TO is indicated by the width of the gray band.

rapidly for $M_V \geq -6.5$ mag. They identified these relatively fainter clusters as belonging to a second population, which is statistically more extended than the brighter population, the so-called faint fuzzies (e.g., [Larsen & Brodie 2000b](#); [Brodie & Larsen 2002](#); [Peng et al. 2006](#); [Liu et al. 2016](#)). They discuss these red extended clusters as old stellar clusters formed in the disk. Only 98 (i.e. 30%) of their clusters belonged to the brighter population, the classical GCs. Our selection criteria, which selects objects $2.4 < \text{FWHM} < 10$ pixel, naturally rejects extended objects that [Simanton et al. \(2015\)](#) have found, but contains compact objects fainter than their magnitude cut of $M_V \geq -6.5$ mag. The fainter TO we have found suggests that our sample is dominated by a population of red faint compact clusters of ages between ~ 1 –10 Gyr. These properties correspond to relatively low-mass reddened SSCs in the disk of M101.

5.5 Physical parameters that control TO

The TO magnitude of a GC system is controlled by four physical parameters, namely, the mass function (MF) at birth, age, metallicity and internal extinction. In addition to these, a dynamical process changes the form of the mass function as the clusters evolve under the gravitational potential of their parent galaxies. At ages greater than a few billion years, dynamical evolution is mass-dependent, which leads to selective destruction of low-mass clusters. In general, a cluster of mass M_{cl} loses all its mass over a time-scale, t_{dis} , given by,

$$t_{dis} = t_4 \left(\frac{M_{cl}}{10^4 M_\odot} \right)^\gamma, \quad (4)$$

where t_4 is the destruction time for a cluster of $10^4 M_\odot$ under a specific gravitational potential, and the power-law index γ is found to have a value of 0.6 ([Boutloukos & Lamers 2003](#)). The t_4 is expected to be shorter in strong gravitational field, such as massive early-type galaxies, and longer, in low-mass late-type galaxies. [Fall & Zhang \(2001\)](#) found that the net

Table 11. Physical parameters corresponding to TO.

Galaxy	Z	Age Gyr	M_{cl}/M_\odot log	σ log
M81	0.0004	13.0	5.58	0.05
	0.001	13.0	5.57	0.05
M101	0.0004	13.0	5.07	0.03
	0.001	13.0	5.06	0.03
NGC4258	0.0004	13.0	5.52	0.04
	0.001	13.0	5.51	0.04
M51	0.0004	13.0	5.55	0.02
	0.001	13.0	5.54	0.02
NGC628	0.0004	13.0	5.50	0.02
	0.001	13.0	5.49	0.02
MW	0.0004	13.0	5.53	0.04
	0.001	13.0	5.52	0.04

result of the dynamical evolution is to create a MF that is log-normal, like the one found in our study, almost independent of the initial form of the MF. The turnover of the resulting MF is shifted to higher masses, equivalently to brighter magnitudes, in early-type galaxies, as compared to the late-type galaxies. Thus, even if the four physical parameters are the same for all GC systems, dynamical evolution alone can introduce dispersion in the observed TOs in different galaxies. The TO is also shifted to higher masses (brighter magnitudes) at longer ages due to dynamical effects.

Using our TO absolute magnitude in the $F814W$ filter, corrected for internal and Galactic extinction ($M_{F814W_0}^{TO}$), we can determine the TO mass of the cluster in our sample of galaxies using an SSP of age and metallicity typical of GCs.

$$\log \mathcal{M} = -0.4 \times (M_{F814W_0}^{TO} - M_{F814W}^{SSP}), \quad (5)$$

where M_{F814W}^{SSP} is the $F814W$ magnitude of an SSP at 13 Gyr for a total mass of $1 M_\odot$. The resulting mass values for two of the lowest metallicities ($Z=0.0004=1/50$ solar and $Z=0.001=1/20$ solar) are given in Table 11. The derived masses are 3% higher for $Z=0.0004$ as compared to that obtained using $Z=0.001$. In the four galaxies with almost universal TO, the mass corresponds to $\sim 3 \times 10^5 M_\odot$, whereas it is lower by a factor two in M101. The disk clusters of M101 are expected to be younger than the uniform age of 13 Gyr we have used. If they are as young as 8 Gyr, the masses will be further lower by $\sim 30\%$.

5.6 Total number of Globular Clusters and Specific frequency

GC searches in external galaxies using HST data are subjected to two kinds of incompleteness: (i) magnitude incompleteness arising due to the missing low-luminosity GCs beyond the detection limit, and (ii) area incompleteness due to non-coverage of outer-halo GCs because of the limited FoV of HST. The alternative strategy of searching GCs in wide-field ground-based surveys also suffers from these two effects, with the second effect arising due to confusion with stellar sources in the inner regions due to lack of spatial resolution. Characterization of the LF and the radial number density distributions with analytical functions, allows us to calculate the total number of GCs by integrating over the

Table 12. Specific frequency.

Galaxy	S_N	$S_{N,TOT}$
M81	0.46 ± 0.10	0.64 ± 0.10
M101 [†]	2.16 ± 0.46	5.35 ± 0.82
NGC 4258	0.57 ± 0.26	1.12 ± 0.30
M51	0.61 ± 0.17	1.48 ± 0.22
NGC 628	0.75 ± 0.17	1.30 ± 0.24

[†]Values estimated assuming the universality of TO applies to M101 are 0.47 ± 0.27 and 0.94 ± 0.33 .

entire range of these functions. We carry out these integrations in two steps, as explained below.

First, we integrate over the fitted GCLF to obtain the number corrected for the missing low-luminosity GCs, which are given in column 3 of Table 10. We define the missing factor, $f_{LF} = N_{GC}(\int LF) / N_{GC}(\text{obs})$. In order to correct for the GCs outside our FoV, we counted the number of GCs within R_e . By definition, total number of detectable GCs is twice this number. The total number of GCs, corrected for contamination from reddened SSCs, and incompleteness both in luminosity and volume is:

$$N_{GC,TOT} = f_{LF} \times 2 \times N'_{GC,R_e}, \quad (6)$$

where N'_{GC,R_e} is listed in the last column in Table 8, which is the number of GCs within R_e corrected for the contamination from reddened young SSCs. In column 4 of Table 10, we tabulate the total number of GCs in each sample galaxy.

The specific frequency, S_N , defined as the number of GCs normalized to the total galaxy magnitude of $M_V = -15$ mag, is related to the $N_{GC,TOT}$ by the relation $S_N = N_{GC,TOT} \times 10^{0.4(M_V + 15)}$ (Harris & van den Bergh 1981). We calculated S_N for each galaxy using the M_V tabulated in Table 1. In Table 12 we show S_N and $S_{N,TOT}$ calculated with $N_{GC,OBS}$ and $N_{GC,TOT}$, respectively. In Figure 19, we show the $S_{N,TOT}$ vs M_V . We also show corresponding values for the MW and M31 (Peacock et al. 2010). The value of S_N for M101 is expected to be an upper limit, given that our GC sample for this galaxy includes a large population of intermediate-age SSCs. We hence made an alternative estimation of S_N , assuming that the true GC population in this galaxy also has the universal TO. We hence counted the number of GCs brighter than $M_V = -7.40$ mag, and doubled that number to calculate $N_{GC,TOT}$. The empty star symbol for M101 in the figure corresponds to this revised S_N . The mean value for our sample, including the revised value of M101 is $\sim 1.10 \pm 0.24$, which occupies a much smaller range as compared to the values for spiral galaxies from the compilation of Harris et al. (2013) (open circles). The large spread in the latter sample is expected as they are based on studies using very different detection and analysis techniques from Fischer et al. (1990), Harris (1996), Kissler-Patig et al. (1999), Harris & Harris (2000), Goudfrooij et al. (2003), Olsen et al. (2004), Rhode & Zepf (2004), Rhode et al. (2007), Di Nino et al. (2009), Mora et al. (2009), Nantais et al. (2010a), Peacock et al. (2010), Rhode et al. (2010), Adamo et al. (2011) and Young et al. (2012).

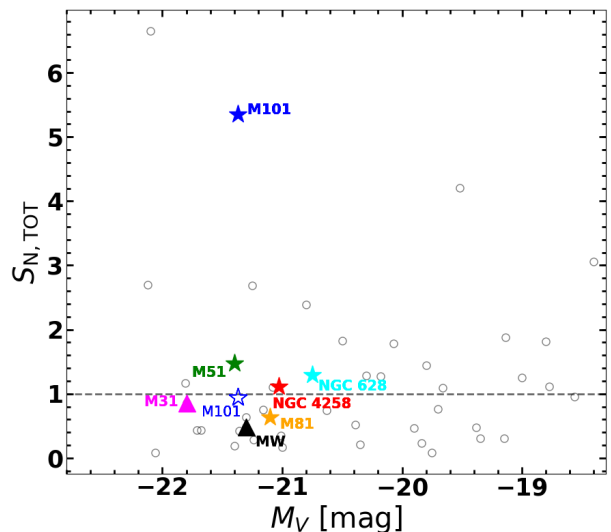


Figure 19. GC specific frequency plotted against the absolute magnitude of the host galaxy for our sample of 5 galaxies (filled star symbol), the MW and M31 (triangles). The empty star symbol for M101 corresponds to the value obtained assuming a universal TO for this galaxy (see text for details). Dashed horizontal line indicates average values for spiral galaxies from the compilation of Harris et al. (2013), which are shown by empty circles.

6 CONCLUSIONS

We used the HST images of five nearby spiral galaxies for which there are data taken with multiple pointings with ACS to enable a search of GCs in them. Images in $F435W$, $F555W$ and $F814W$ filters were used. We used SExtractor and a set of cluster-defining filters to define a sample of GCs in each of the analysed galaxies. Detection of simulated clusters was carried out to obtain the incompleteness as a function of magnitude. We used the U -band photometry for a subset of sample GCs using the SDSS u -band images for M81 and HST/WFC3 $F336W$ images for the rest to evaluate the contamination of our GC samples by reddened SSCs. The contaminating fraction was found to be between 0.14–0.35. We used the dataset to construct luminosity function of GCs in spiral galaxies.

We find that the LF of GCs in all the five galaxies analysed is log-normal in nature, with the turn-over (TO) happening on the brighter side of the 50% incompleteness limit in all galaxies. This has enabled us to determine precise TO magnitudes for our sample of galaxies. We also determined typical internal extinction towards the population of GCs in our sample galaxies by comparing the mode of the observed colours with that from population synthesis models for a metal-poor (metallicity = $1/20^{th}$ solar) population of 13 Gyr. We used the best determined distances for the sample galaxies to convert the extinction corrected V -magnitude corresponding to the turn-over into the absolute magnitude $M_{V0}(TO)$ and obtained errors on this by carrying out Monte Carlo simulations. The mean of the $M_{V0}(TO)$ in 4 of our galaxies is -7.41 ± 0.14 , which is in excellent agreement with the values determined for GC population in the Milky Way of $M_{V0}(TO)_{MW} = -7.40 \pm 0.10$. In the fifth galaxy M101, $M_{V0}(TO)$ is 1.16 mag fainter than that for the MW. We

propose that this difference in $M_{V0}(\text{TO})$ arises due to morphological differences, with spiral galaxies of the Hubble types Sc or earlier having a universal $M_{V0}(\text{TO})$, whereas the Hubble types later than Sc have fainter $M_{V0}(\text{TO})$. The universality of $M_{V0}(\text{TO})$ in early-type spirals is due to the classical GCs dominating the GC population, whereas in late-type spirals GC population is often dominated by old disk clusters, which are in general less massive, and hence fainter than the classical GCs, but otherwise share the same observational properties as the classical GCs. The universal TO value corresponds to a stellar mass of $\sim 3 \times 10^5 M_{\odot}$, where the corresponding value is a factor of 2 lower for M101.

We used the dataset of GCs to address three other topics of interest, namely the form of the radial density distribution, distribution of colours, and the specific number density. The Sérsic function with index between $n=0.36$ – 1.63 is a good fit for the radial density distribution of GCs in our sample of galaxies. The index value suggests exponential form, rather than the much steeper $n=3$ – 4 form found in elliptical galaxies (Kantha et al. 2014). We carried out a statistical analysis of $(B - I)_0$, $(B - V)_0$ and $(V - I)_0$ colour distributions for our sample of 5 galaxies. We found that the correction factor for contaminating reddened SSCs is a function of GC colour. Taking into account the errors in this correction factor, we find no compelling evidence for a bimodal distribution. We have calculated N_{GC} , the total number of GCs by making corrections for undetected faint sources, and those outside of our FoV, by extrapolating the GCLF to fainter magnitude and radial surface density profiles to outside our FoV, respectively. The specific number density $S_N \sim 1.10 \pm 0.24$ for our sample of spiral galaxies.

ACKNOWLEDGEMENTS

We are grateful to two anonymous referees for their valuable suggestions on the original manuscript, especially for suggesting us to carryout corrections for possible contamination of our GC samples from reddened young clusters. LLN thanks CONACyT for granting PhD research fellowship that enabled him to carry out the work presented here. We also thank CONACyT for the research grants CB-A1-S-25070 (YDM), and CB-A1-S-22784 (DRG).

This work has made use of data from the European Space Agency (ESA) mission *Gaia* (<https://www.cosmos.esa.int/gaia>), processed by the *Gaia* Data Processing and Analysis Consortium (DPAC, <https://www.cosmos.esa.int/web/gaia/dpac/consortium>). Funding for the DPAC has been provided by national institutions, in particular the institutions participating in the *Gaia* Multilateral Agreement.

DATA AVAILABILITY

The data underlying this article are available in the article and in its online supplementary material.

REFERENCES

Adamo A., Östlin G., Zackrisson E., Hayes M., 2011, *MNRAS*, **414**, 1793

- Adamo A., et al., 2017, *ApJ*, **841**, 131
 Alamo-Martínez K. A., et al., 2013, *ApJ*, **775**, 20
 Ashman K. M., Zepf S. E., 1998, Cambridge Astrophysics Series, **30**
 Ashman K. M., Bird C. M., Zepf S. E., 1994, *AJ*, **108**, 2348
 Barmby P., Kuntz K. D., Huchra J. P., Brodie J. P., 2006, *AJ*, **132**, 883
 Bassino L. P., Richtler T., Dirsch B., 2006, *MNRAS*, **367**, 156
 Bastian N., 2008, *MNRAS*, **390**, 759
 Bastian N., et al., 2011, *MNRAS*, **417**, L6
 Battistini P. L., Bonoli F., Casavecchia M., Ciotti L., Federici L., Fusi-Pecchi F., 1993, *A&A*, **272**, 77
 Bertin E., Arnouts S., 1996, *A&AS*, **117**, 393
 Bessell M. S., 1990, *PASP*, **102**, 1181
 Bica E., Bonatto C., Barbay B., Ortolani S., 2006, *A&A*, **450**, 105
 Binney J., Merrifield M., 1998, Galactic Astronomy
 Boutloukos S. G., Lamers H. J. G. L. M., 2003, *MNRAS*, **338**, 717
 Brodie J. P., Larsen S. S., 2002, *AJ*, **124**, 1410
 Brodie J. P., Strader J., 2006, *ARA&A*, **44**, 193
 Bruzual G., Charlot S., 2003, *MNRAS*, **344**, 1000
 Burkert A., Tremaine S., 2010, *ApJ*, 720
 Cantiello M., Grado A., Rejkuba M., Arnaboldi M., Capaccioli M., Greggio L., Iodice E., Limatola L., 2017, preprint, ([arXiv:1711.00805](https://arxiv.org/abs/1711.00805))
 Cardelli J. A., Clayton G. C., Mathis J. S., 1989, *ApJ*, **345**, 245
 Chandar R., Whitmore B., Lee M. G., 2004, *ApJ*, **611**, 220
 Cohen J. G., Blakeslee J. P., Ryzhov A., 1998, *ApJ*, **496**, 808
 Corwin Jr. H. G., Buta R. J., de Vaucouleurs G., 1994, *AJ*, **108**, 2128
 Côté P., Marzke R. O., West M. J., 1998, *ApJ*, **501**, 554
 Di Nino D., Trenti M., Stiavelli M., Carollo C. M., Scarlata C., Wyse R. F. G., 2009, *AJ*, **138**, 1296
 Fall S. M., Zhang Q., 2001, *ApJ*, **561**, 751
 Fedotov K., Gallagher S. C., Konstantopoulos I. S., Chandar R., Bastian N., Charlton J. C., Whitmore B., Trancho G., 2011, *AJ*, **142**, 42
 Fischer P., Hesser J. E., Harris H. C., Bothun G. D., 1990, *PASP*, **102**, 5
 Gaia Collaboration et al., 2016, *A&A*, **595**, A1
 Gaia Collaboration et al., 2018, *A&A*, **616**, A1
 Gebhardt K., Kissler-Patig M., 1999, *AJ*, **118**, 1526
 Georgiev I. Y., Hilker M., Puzia T. H., Chanamé J., Mieske S., Goudfrooij P., Reisenegger A., Infante L., 2006, *A&A*, **452**, 141
 Georgiev I. Y., Puzia T. H., Goudfrooij P., Hilker M., 2010, *MNRAS*, **406**, 1967
 Gieles M., Baumgardt H., Heggie D. C., Lamers H. J. G. L. M., 2010, *MNRAS*, **408**, L16
 González-Lópezlira R. A., et al., 2017, *ApJ*, **835**, 184
 González-Lópezlira R. A., et al., 2019, *ApJ*, **876**, 39
 Goudfrooij P., Strader J., Brenneman L., Kissler-Patig M., Minniti D., Edwin Huizinga J., 2003, *MNRAS*, **343**, 665
 Hanes D. A., 1977a, Mem. RAS, **84**, 45
 Hanes D. A., 1977b, *MNRAS*, **180**, 309
 Hargis J. R., Rhode K. L., 2014, *ApJ*, **796**, 62
 Harris W. E., 1996, *AJ*, **112**, 1487
 Harris H. C., Harris W. E., 2000, Star Clusters. p. 545
 Harris G. L. H., Harris W. E., 2011, *MNRAS*, **410**, 2347
 Harris W. E., van den Bergh S., 1981, *AJ*, **86**, 1627
 Harris W. E., Harris G. L. H., Alessi M., 2013, *ApJ*, **772**, 82
 Harris W. E., et al., 2014, *ApJ*, **797**, 128
 Hwang N., Lee M. G., 2008, *AJ*, **135**, 1567
 Jang I. S., Lim S., Park H. S., Lee M. G., 2012, *ApJ*, **751**, L19
 Jang I. S., de Jong R. S., Holwerda B. W., Monachesi A., Bell E. F., Bailin J., 2020, arXiv e-prints, p. [arXiv:2001.12007](https://arxiv.org/abs/2001.12007)
 Jordán A., et al., 2007, *ApJS*, **171**, 101

Kartha S. S., Forbes D. A., Spitler L. R., Romanowsky A. J., Arnold J. A., Brodie J. P., 2014, *MNRAS*, **437**, 273

Kissler-Patig M., Ashman K. M., Zepf S. E., Freeman K. C., 1999, *AJ*, **118**, 197

Kormendy J., Drory N., Bender R., Cornell M. E., 2010, *ApJ*, **723**, 54

Kundu A., Whitmore B. C., 1998, *AJ*, **116**, 2841

Larsen S. S., Brodie J. P., 2000a, *AJ*, **120**, 2938

Larsen S. S., Brodie J. P., 2000b, *AJ*, **120**, 2938

Larsen S. S., Brodie J. P., Huchra J. P., Forbes D. A., Grillmair C. J., 2001, *AJ*, **121**, 2974

Liu Y., Peng E. W., Lim S., Jordán A., Blakeslee J., Côté P., Ferrarese L., Pattarakijwanich P., 2016, *ApJ*, **830**, 99

Ma J., et al., 2017, *MNRAS*, **468**, 4513

Mackey A. D., Gilmore G. F., 2003, *MNRAS*, **338**, 85

Macri L. M., et al., 2001, *ApJ*, **549**, 721

Mamikonian E. N., McMillan S. L. W., Vesperini E., Mac Low M.-M., 2017, *ApJ*, **837**, 70

Mayya Y. D., Romano R., Rodríguez-Merino L. H., Luna A., Carrasco L., Rosa-González D., 2008, *ApJ*, **679**, 404

Mayya Y. D., Rosa-González D., Santiago-Cortés M., Rodríguez-Merino L. H., Vega O., Torres-Papaqui J. P., Bressan A., Carrasco L., 2013, *MNRAS*, **436**, 2763

McLaughlin D. E., Harris W. E., Hanes D. A., 1994, *ApJ*, **422**, 486

Mora M. D., Larsen S. S., Kissler-Patig M., Brodie J. P., Richtler T., 2009, *A&A*, **501**, 949

Muñoz R. P., et al., 2014, *ApJS*, **210**, 4

Nantais J. B., Huchra J. P., McLeod B., Strader J., Brodie J. P., 2010a, *AJ*, **139**, 1413

Nantais J. B., Huchra J. P., McLeod B., Strader J., Brodie J. P., 2010b, *AJ*, **139**, 1413

O’Connell R. W., Gallagher III J. S., Hunter D. A., Colley W. N., 1995, *ApJ*, **446**, L1

Olivares E. F., et al., 2010, *ApJ*, **715**, 833

Olsen K. A. G., Miller B. W., Suntzeff N. B., Schommer R. A., Bright J., 2004, *AJ*, **127**, 2674

Peacock M. B., Maccarone T. J., Knigge C., Kundu A., Waters C. Z., Zepf S. E., Zurek D. R., 2010, *MNRAS*, **402**, 803

Peng E. W., et al., 2006, *ApJ*, **639**, 838

Peng E. W., et al., 2008, *ApJ*, **681**, 197

Perelmuter J.-M., Racine R., 1995, *AJ*, **109**, 1055

Reed L. G., Harris G. L. H., Harris W. E., 1994, *AJ*, **107**, 555

Reid M. J., Pesce D. W., Riess A. G., 2019, *ApJ*, **886**, L27

Rhode K. L., Zepf S. E., 2004, *AJ*, **127**, 302

Rhode K. L., Zepf S. E., Kundu A., Larner A. N., 2007, *AJ*, **134**, 1403

Rhode K. L., Windschitl J. L., Young M. D., 2010, *AJ*, **140**, 430

Richtler T., 2003, in Alloin D., Gieren W., eds, *Lecture Notes in Physics*, Berlin Springer Verlag Vol. 635, *Stellar Candles for the Extragalactic Distance Scale*. pp 281–305 ([arXiv:astro-ph/0304318](https://arxiv.org/abs/astro-ph/0304318)), doi:10.1007/978-3-540-39882-0_15

Riess A. G., et al., 2016, *ApJ*, **826**, 56

Rodríguez Ó., Clocchiatti A., Hamuy M., 2014, *AJ*, **148**, 107

Ryon J. E., et al., 2017, *ApJ*, **841**, 92

Santiago-Cortés M., Mayya Y. D., Rosa-González D., 2010, *MNRAS*, **405**, 1293

Schlafly E. F., Finkbeiner D. P., 2011, *ApJ*, **737**, 103

Secker J., 1992, *AJ*, **104**, 1472

Sersic J. L., 1968, *Atlas de Galaxias Australes*

Simanton L. A., Chandar R., Whitmore B. C., 2015, *ApJ*, **805**, 160

Sirianni M., et al., 2005, *PASP*, **117**, 1049

Stetson P. B., 1987, *PASP*, **99**, 191

Tully R. B., et al., 2013, *AJ*, **146**, 86

Usher C., et al., 2012, *MNRAS*, **426**, 1475

Webb J. J., Harris W. E., Sills A., 2012, *ApJ*, **759**, L39

West M. J., Côté P., Marzke R. O., Jordán A., 2004, *Nature*, **427**, 31

Whitmore B. C., Schweizer F., 1995, *AJ*, **109**, 960

Whitmore B. C., Sparks W. B., Lucas R. A., Macchetto F. D., Biretta J. A., 1995, *ApJ*, **454**, L73

Whitmore B. C., Chandar R., Bowers A. S., Larsen S., Lindsay K., Ansari A., Evans J., 2014, *AJ*, **147**, 78

Young M. D., Dowell J. L., Rhode K. L., 2012, *AJ*, **144**, 103

Zepf S. E., Ashman K. M., 1993, *MNRAS*, **264**, 611

APPENDIX A: COMPARISON WITH THE HLA CATALOGS

We started our work using the SExtractor catalogs for cluster selection, available at the Hubble Legacy Archive (HLA). With our method of selection, we expect that an object has at least $AREA=50$ pixels to be considered as candidate for a star cluster. We found that $AREA$ values reported in HLA catalogs: 02, a2 and 11 of M101 are very small, with very few objects having $AREA > 50$ pixel. On other fields of the same galaxy, there were sources having $AREA > 50$ pixel. In order to understand the absence of sources having $AREA > 50$ pixel, we downloaded the images and ran the SExtractor using the same input file as that used by the HLA.

In top Figure A1, we show a comparison between MAG_{ISO} (top row) and $AREA$ (bottom row) of HLA catalogs and SExtractor catalogues obtained by us in $F814W$ -band. The histograms of both the quantities compare very well. However, HLA MAG_{ISO} is systematically fainter and the $AREA$ systematically smaller than the values we obtained, and hence the observed differences in fields 02, a2, 11 for M101 can be directly understood in terms of an underestimation of background in the HLA catalogues.

The distribution of the SExtractor parameters available at HLA coincided with that obtained from our own runs of SExtractor for all other frames where we made a comparison. However, in order to ensure uniform analysis of all sample galaxies, we downloaded the fits files and generated our own catalogues for each frame. The discussion presented here serves as a cautionary note while planning to use the HLA catalogues for quantitative scientific studies.

APPENDIX B: TRANSFORMATION TO JOHNSON-COUSINS SYSTEM

Majority of the photometric data for GCs in the MW and external galaxies are reported in the standard Johnson-Cousins $UBVRI$ system (Bessell 1990). Hence, in order to compare the results obtained from our study to that obtained in other galaxies, it is necessary to transform our $F435W$, $F555W$ and $F814W$ magnitudes and colours into the standard system. The corresponding transformation equations are discussed in detail by Sirianni et al. (2005). The transformation from a HST system (SOURCE), to a TARGET system (T), in our case, the Johnson-Cousins $UBVRI$ system, is given by:

$$TMAG = SMAG + c0 + c1 \times TCOL + c2 \times TCOL^2, \quad (B1)$$

where $SMAG$ and $TMAG$ are the magnitudes in the source and target systems, respectively, $TCOL$ is the colour in the

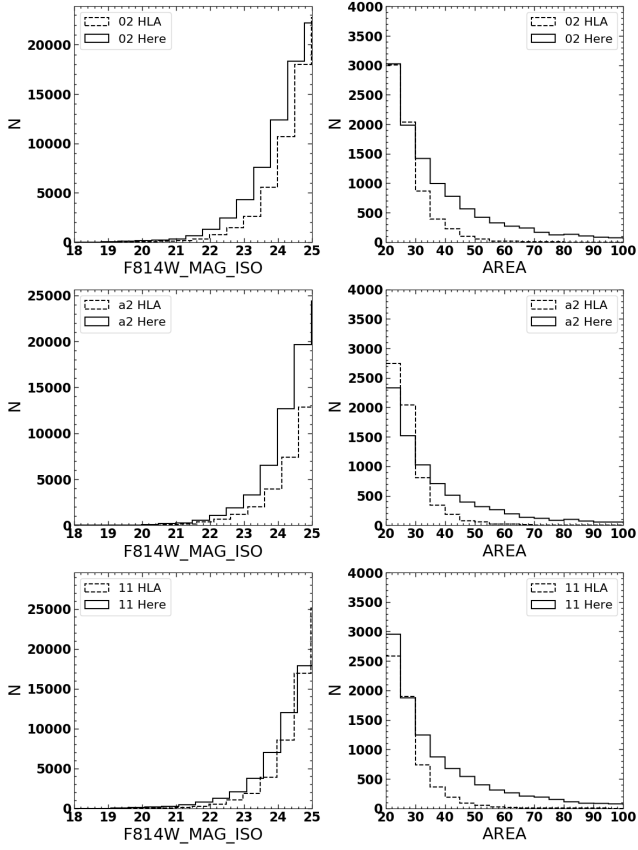


Figure A1. Frames covering M101 with incorrect values of AREA and MAG_ISO values in the source catalogues of HLA. The frame numbers for set are indicated. Dashed histograms show the values from the HLA catalogues, whereas the solid histograms show values from our catalogue, using the same SExtractor input file as for the HLA catalogue.

Table B1. Transformation coefficients between HST and Johnson-Cousins systems.

HST	UBVRI	TCOL	c1	c2	Range
F435W	<i>B</i>	$B - I$	0.022 ± 0.006	-0.038 ± 0.011	<1.0
F435W	<i>B</i>	$B - I$	0.008 ± 0.006	-0.005 ± 0.001	>1.0
F555W	<i>V</i>	$B - V$	-0.083 ± 0.032	0.020 ± 0.115	<0.2
F555W	<i>V</i>	$B - V$	-0.087 ± 0.007	0.004 ± 0.002	>0.2
F814W	<i>I</i>	$B - I$	0.013 ± 0.006	-0.028 ± 0.112	<0.3
F814W	<i>I</i>	$B - I$	-0.010 ± 0.010	-0.006 ± 0.002	>0.3
F606W	<i>V</i>	$B - V$	0.170 ± 0.005	0.061 ± 0.002	...

target system in the chosen bands, c_0 is the zeropoint, which is taken from Table 2 for the respective frames, c_1 and c_2 are the first and second order colour coefficients, whose values for the colour ranges of interest in this study are given in Table B1. Since TCOLs are in the TARGET system, their values are assumed to be the same as in the HST system to start with, which are updated iteratively, until the value of TCOLs converges.

This paper has been typeset from a $\text{\TeX}/\text{\LaTeX}$ file prepared by the author.